



A Combined Cosmogenic Nuclides Approach for Determining the Temperature-Dependence of Erosion

Donovan P. Dennis¹ and Dirk Scherler^{1,2} ¹Helmholtz Centre Potsdam GFZ German Research Centre for Geosciences, Potsdam, Germany, ²Institute of Geological Sciences, Freie Universität Berlin, Berlin, Germany**Key Points:**

- Cosmogenic ¹⁰Be, ¹⁴C, and ³He is used to determine erosion rates, erosion styles, and bedrock temperatures in cold regions
- ¹⁴C/¹⁰Be ratios of surface samples reflect the depth at which material was previously eroded, allowing for determination of erosion style
- ¹⁴C/¹⁰Be ratios combined with ¹⁰Be-derived erosion rates improve erosion rate estimates in stochastically eroding environments

Correspondence to:D. P. Dennis,
dennis@gfz-potsdam.de**Citation:**Dennis, D. P., & Scherler, D. (2022). A combined cosmogenic nuclides approach for determining the temperature-dependence of erosion. *Journal of Geophysical Research: Earth Surface*, 127, e2021JF006580. <https://doi.org/10.1029/2021JF006580>Received 23 DEC 2021
Accepted 11 MAR 2022

Abstract Physical weathering in cold, steep bedrock hillslopes occurs at rates that are thought to depend on temperature, but our ability to quantify the temperature-dependence of erosion remains limited when integrating over geomorphic timescales. Here, we present results from a 1D numerical model of in-situ cosmogenic ¹⁰Be, ¹⁴C, and ³He concentrations that evolve as a function of erosion rate, erosion style, and ground surface temperature. We used the model to explore the suitability of these nuclides for quantifying erosion rates in areas undergoing non-steady state erosion, as well as the relationship between bedrock temperature, erosion rate, and erosional stochasticity. Our results suggest that even in stochastically eroding settings, ¹⁰Be-derived erosion rates of amalgamated samples can be used to estimate long-term erosion rates, but infrequent large events can lead to bias. The ratio of ¹⁴C to ¹⁰Be can be used to evaluate erosional stochasticity, and to determine the offset between an apparent ¹⁰Be-derived erosion rate and the long-term rate. Finally, the concentration of ³He relative to that of ¹⁰Be, and the paleothermometric interpretations derived from it, are unaffected by erosional stochasticity. These findings, discussed in the context of bedrock hillslopes in mountainous regions, indicate that the ¹⁰Be-¹⁴C-³He system in quartz offers a method to evaluate the temperature-sensitivity of bedrock erosion rates in cold, high-alpine environments.

Plain Language Summary All mountains erode, but not all mountains erode in the same way and at the same rate. In cold mountainous landscapes, temperature is thought to be an important control on erosion. Previous research suggests that rocks fracture by frost most effectively at temperatures between -3°C and -8°C , and that the warming and thawing of permanently frozen ground (permafrost) destabilizes hillslopes and leads to more and larger rockfalls. However, our ability to test these hypotheses is limited, due to difficulties in measuring or estimating erosion rates and linking them with the temperatures that rocks experience. In this paper we present the results of a computer modeling study that tests the suitability of geochemical tools as measures of erosion rate, erosion style, and long-term bedrock temperature. We find that these geochemical tracers, called cosmogenic nuclides, can be used to determine erosion rates, even in places that are prone to rare rockfalls, together with the long-term bedrock temperature. They are therefore uniquely suitable for evaluating the link between temperatures and erosion rates in cold bedrock hillslopes over long timescales.

1. Introduction

Cold, alpine regions are among the environments most sensitive to changes in temperature and climate. Anthropogenic global warming throughout the last century has induced widespread geomorphic destabilization within these cold regions, notably through the retreat of alpine glaciers and the thawing of mountain permafrost. Both glacial retreat and permafrost thaw are believed to increase the frequency of rockfalls and other slope failures, threatening humans as well as infrastructure (Gruber et al., 2004a; Noetzi et al., 2003; Ravelin & Deline, 2011). Assessing the vulnerability of steep bedrock hillslopes to potential slope failures is therefore an important prerequisite for mitigating the long-term effects of climate change in alpine regions. Our understanding of the environmental controls on erosion mechanisms in these regions is limited, however, in part because we lack robust estimates of long-term background erosion rates.

Frost-cracking and rockfalls induced by the thawing of permafrost are considered primary mechanisms of physical weathering and erosion in cold, bedrock hillslopes (Hales & Roering, 2005, 2009; Matsuoka & Murton, 2008; Scherler, 2014). First seeded as thin films of ice in pre-existing bedrock fractures, segregation ice wedges expand as liquid water is drawn to the ice and subsequently frozen onto its surface (Hallet et al., 1991). Theoretical considerations (Walder & Hallet, 1985) and experiments (Murton et al., 2006) suggest that with sufficient liquid

© 2022 The Authors.

This is an open access article under the terms of the [Creative Commons Attribution-NonCommercial License](https://creativecommons.org/licenses/by-nc/4.0/), which permits use, distribution and reproduction in any medium, provided the original work is properly cited and is not used for commercial purposes.

water available, bedrock temperatures between approximately -8°C and -3°C (the “frost-cracking window” of Anderson (1998)) promote rapid rock fracture. In addition to fracturing rock following their expansion, the eventual thawing of ice wedges and ice lenses in bedrock permafrost is believed to be responsible for recent increases in rockfalls. Studies of rockfall activity in alpine permafrost zones have shown that short periods of extreme heat or prolonged periods of moderate heat often precede enhanced rockfall activity (e.g., Bodin et al., 2015; Gallach et al., 2018, 2020; Ravelle & Deline, 2011). Bedrock temperature therefore plays a key role in determining the spatial distribution and magnitude of erosion in cold, bedrock hillslopes. Testing the temperature-dependence of erosion remains difficult, however, particularly for the “frost-cracking window” hypothesis, given that long-term empirical data is sparse (Matsuoka & Murton, 2008).

Because of the biases inherent when estimating erosion rates over hundreds to thousands of years, relatively little is known about long-term bedrock erosion rates in cold regions (e.g., Ganti et al., 2016). Most previous studies of frost-cracking and bedrock hillslope erosion use short-term observations of rock fracture dynamics (e.g., Matsuoka, 2019) or long-term, indirect observations, such as talus slope accumulation/morphology (e.g., Hinchcliffe & Ballantyne, 1999, 2009; Siewert et al., 2012). Assumptions about rockfall source area, talus stability, regional paleoclimate conditions, and, if applicable, local deglaciation timescale, all contribute to uncertainty in long-term erosion rate estimations. High-resolution datasets of temperature and erosion events in permafrost regions (e.g., Harris et al., 2009; PERMOS, 2001) on the other hand, integrate over annual or, more rarely, decadal timescales (Savi et al., 2021), but they may not incorporate stochastic events that occur at centennial or lower frequency, thereby underestimating long-term erosion rates. Similarly, inclusion of a large event within a narrow timeframe of integration artificially increases erosion rates when interpreted as representing the long-term. In contrast, estimations of erosion rates derived from sediment accumulation in down-stream lakes or basins (Hinderer, 2001) or ^{10}Be -derived catchment-averaged erosion rates (e.g., Wittmann et al., 2007) may reflect long-term erosion more accurately, but linking rates with specific processes, such as frost-cracking, is not straightforward. Studying smaller sedimentary deposits, such as talus slopes, can reduce uncertainty about the rockfall source area, but erosion rate determination nevertheless relies on integration times inferred from geomorphologic or stratigraphic evidence, such as an assumed deglaciation time, rather than discrete measurements (e.g., Sass & Wollny, 2001). Talus slope and debris-net accumulation-derived rates are therefore subject to substantial uncertainties which may span orders of magnitude (e.g., Gray, 1971; Hollermann, 1983; Olyphant, 1983).

Recently, researchers have employed new methods to study these landscapes, including using cosmogenic nuclides (CN). For example, Mair et al. (2019) derived bedrock erosion rates from ^{36}Cl concentrations measured in several (<10 m long) depth profiles. While their study yielded unique insights, the extent to which these measurements are representative is limited by their spatial coverage. Gallach et al. (2018, 2020), on the other hand, collected surface samples from several exposed peaks in the Mont Blanc massif, taking care to ensure a large spatial coverage—but they interpreted ^{10}Be concentrations as surface exposure ages. Ward and Anderson (2011) collected amalgamated samples from medial moraines that act “as samplers for ^{10}Be -derived erosion rates of glacier valley walls,” thereby integrating over large areas, but requiring the presence of a glacier. Sarr et al. (2019) conducted a careful analysis of supraglacial debris in the Mont Blanc Massif, concluding that ^{10}Be -derived erosion rates of rockfall-prone regions prove useful so long as the number of clasts included in the amalgamated sample represents more than 30 rockfalls. The above studies demonstrate that opportunities exist to quantify long-term erosion rates in cold and steep bedrock hillslopes, but that difficult access and the stochastic nature of rockfalls pose challenges.

Here, we explore the utility of three CN produced in quartz for evaluating the temperature sensitivity and long-term erosional behavior of cold, bedrock hillslopes using a 1D numerical model. We build on existing applications of *in-situ*-produced cosmogenic ^{10}Be , ^{14}C , and ^3He , incorporating cosmogenic nuclide production, decay, and diffusion, alongside temperature conditions in the shallow sub-surface bedrock. Because of its slow rate of decay, ^{10}Be concentrations in quartz can be used for estimating erosion rates on long (kyr) timescales (Lal, 1991). When ^{14}C is measured in parallel with ^{10}Be , the ratio of ^{14}C to ^{10}Be reflects the relative depth of an erosional event due to differences in the relative production rates at depth (Lupker et al., 2015). ^{14}C is therefore potentially suitable for discriminating recent deep-seated slope failures from shallow surface events when paired with a nuclide that decays more slowly. Finally, rates of simultaneous production and diffusion of cosmogenic ^3He depend primarily on the bedrock thermal history. Concentrations of ^3He relative to ^{10}Be have previously been used to estimate long-term environmental temperature conditions in non- and very slowly eroding (0.0001–

0.005 mm yr⁻¹) environments (Tremblay et al., 2014a). We apply these principles here to more rapidly eroding regimes (0.5 mm yr⁻¹ to 2.5 mm yr⁻¹). This combination of nuclides has not yet been tested in stochastically eroding settings. It is therefore unclear whether they are equally suitable for the variety of erosion regimes expected in high-alpine regions. Our model simulations allow us to evaluate the response of these proxies to different erosion rates and to assess their utility for studying stochastic erosional processes in steep, bedrock hillslopes.

2. Theoretical Background

Cosmic rays are charged particles with high kinetic energy that constantly bombard the Earth's atmosphere and surface, initiating a cascade of nuclear reactions during their interaction with other particles (Lal, 1991). These nuclear reactions produce CN, including ¹⁰Be, ¹⁴C, and ³He in quartz Gosse & Philips, 2001; Niedermann, 2002). Nuclide production at depths greater than 10 m is mostly negligible due to the attenuation of the cosmic ray flux in the subsurface (Dunai, 2010; Lal, 1991). For most nuclides, mineral-specific production rates are well-constrained, making them useful tracers of Earth surface processes (Bierman, 1994; Gosse & Philips, 2001; Lal, 1991; von Blanckenburg & Willenbring, 2014). Because of its abundance in crustal (silicate) rocks, and its capacity to produce multiple nuclides of interest, quartz is a useful and commonly used mineral.

2.1. Production and Decay of ¹⁰Be and ¹⁴C in Quartz

Nearly all cosmogenic ¹⁰Be in quartz is produced via spallation reactions in the uppermost three m of the Earth's surface at a rate decreasing exponentially with depth:

$$P_n(z) = P_n(0) \exp\left(\frac{-z \rho_{rock}}{\Lambda_n}\right) \quad (1)$$

where $P_n(z)$ is the production rate (atoms g⁻¹ yr⁻¹) due to spallation at depth z (cm), $P_n(0)$ the surface production rate (atoms g⁻¹ yr⁻¹) of the nuclide of interest, ρ the rock overburden density (g cm⁻³), and Λ_n the attenuation length scale (g cm⁻²) (Lal, 1991). A small, though quantifiable, amount of cosmogenic ¹⁰Be is additionally produced via both negative and fast muon capture. Negative muon capture production rates can be approximated as

$$P_{\mu^-}(z) = R_{\mu^-}(z) f_{tot} \quad (2)$$

where $P_{\mu^-}(z)$ is the negative muon capture production rate at depth z , $R_{\mu^-}(z)$ the stopping rate (μ-g⁻¹ yr⁻¹) of negative muons and f_{tot} is the probability of the nuclide production per stopped negative muon (Heisinger et al., 2002; Lupker et al., 2015). The stopping rate of negative muons can be approximated by

$$R_{\mu^-}(z) = A_1 \exp\left(\frac{-z \rho_{rock}}{\Lambda_{\mu,1}}\right) + A_2 \exp\left(\frac{-z \rho_{rock}}{\Lambda_{\mu,2}}\right) \quad (3)$$

where $A_1 = 170.6$ and $A_2 = 36.75$ g⁻¹ yr⁻¹ at sea level high latitude (SLHL) and $\Lambda_{\mu,1} = 738.6$ g cm⁻² and $\Lambda_{\mu,2} = 2,688$ g cm⁻² (Granger & Smith, 2000; Stone et al., 1998). Production by fast muon reaction can be approximated as the exponential

$$P_{\mu^f} = B \exp\left(\frac{-\rho_{rock} z}{\Lambda_{\mu,3}}\right) \quad (4)$$

where $B = 0.026$ atoms g⁻¹ yr⁻¹ for ¹⁰Be at SLHL and $\Lambda_{\mu,3}$ is 4,360 g cm⁻² (Granger & Smith, 2000). Accounting for radioactive decay, and including accumulation due to stopped negative muons, the concentration of radiogenic nuclides (C) at time (t), is

$$C(z, t) = C_{inh} e^{-\frac{t}{\tau}} + \int_0^t [P_n(z + \rho \epsilon t') + P_{\mu^-}(z + \rho \epsilon t') + P_{\mu^f}(z + \rho \epsilon t')] e^{-\frac{t-t'}{\tau}} dt' \quad (5)$$

where C_{inh} is the inherited nuclide concentration, τ is the nuclide meanlife, and ϵ the steady-state erosion rate (g cm⁻² yr⁻¹) (Granger & Smith, 2000).

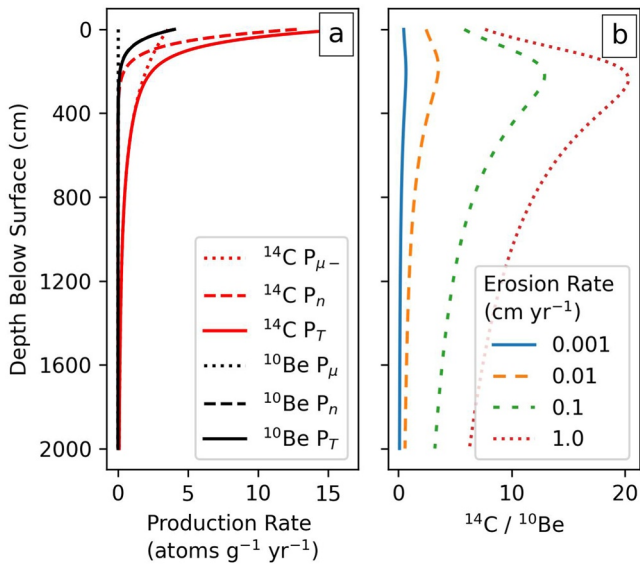


Figure 1. Variations of ¹⁴C and ¹⁰Be production rates with depth, distinguished by production mechanism (spallogenic, P_n ; muogenic, P_μ , or muogenic via negative muon capture, P_{μ^-} ; total, P_T) (a). Surface production rates correspond to sea-level and high latitude. Variation of the ¹⁴C/¹⁰Be ratio with depth as a function of the (uniform) erosion rate (b).

¹⁴C in quartz is produced via spallation reactions and negative muon capture (Equations 1 and 2). But unlike ¹⁰Be, the contribution of negative muon capture to the total ¹⁴C production rate is higher—around 20% of the total surface ¹⁴C production rate (Lupker et al., 2015). When measured together, the two nuclides can yield additional information about temporal changes in erosion rates, as well as evidence for rapid exhumation events in the past (Hippe et al., 2019, 2021). Surficial ¹⁴C/¹⁰Be ratios are set by the erosion rate. At low erosion rates (<0.01 cm yr⁻¹) the exhumation of rock enriched in ¹⁴C relative to ¹⁰Be cannot compensate for the decay of ¹⁴C at the surface, and the ¹⁴C/¹⁰Be ratio is lower than the surface production rate ratio (Figure 1b). At fast erosion rates (>1.0 cm yr), the ¹⁴C/¹⁰Be ratio is higher than the surface production rate ratio due to the rapid exhumation of material enriched in muogenically produced ¹⁴C nuclides from below (Figure 1c). ¹⁴C/¹⁰Be is additionally sensitive to short term deviations from the long-term average erosion rate (Hippe et al., 2019; Yanites et al., 2009), in that recent rapid erosion events (e.g., rockfalls or landslides) are recorded by the ¹⁴C/¹⁰Be ratio. Below we explore the sensitivity of this ratio for determining the prevalence of rapid erosion events.

2.2. Production and Diffusion of ³He in Quartz

As a quartz grain accumulates *in situ*-produced cosmogenic ³He, atoms of ³He simultaneously diffuse out of the quartz grain at a temperature-dependent rate. Production of ³He occurs overwhelmingly via spallation reactions (Vermeesch et al., 2009), though numerical modeling (Lal, 1987) and limited geological evidence suggests that muogenic production of ³He also occurs in small quantities (less than 3 % of spallogenic surface production) in pyroxenes (Larsen et al., 2021). Given the dearth of suitable calibration data and its presumably low contribution to the total production rate, we do not include muogenic production of ³He in the model. For a given temperature T (K), the rate of change in the concentration (C_{3He}) of ³He in a quartz grain can be described with the 2D spherical heat equation:

$$\frac{\partial C_{3He}}{\partial t} = \frac{D(T)}{a^2} \nabla^2 C_{3He} + P_{n,3He} \quad (6)$$

where $D(T)$ is the diffusivity as a function of temperature (cm² s⁻¹), a is the dimension of the diffusion domain, ∇ the Laplace operator, and $P_{n,3He}$ is the spallogenic surface production rate of ³He in quartz. The diffusivity of ³He within a quartz grain is determined by

$$\frac{D(T)}{a^2} = \frac{D_0}{a^2} \exp\left(\frac{-E_a}{RT(T)}\right) \quad (7)$$

where D_0 is the ³He diffusivity in quartz at infinite temperature (cm² s⁻¹), E_a is the activation energy (J mol⁻¹), and R is the gas constant (J K⁻¹ mol⁻¹). The diffusivity term is specific to the kinetic parameters of the mineral grains considered. In our model, we used the diffusion kinetic parameters (E_a and $\ln(D_0/a)$) reported by Shuster and Farley (2005), although these parameters can vary for different species of quartz (Tremblay et al., 2014b) and should be determined independently for each individual field application. Because diffusivity is a function of temperature, it cannot be considered constant with time, and must take changes in temperature into account. Here we calculate an “effective diffusivity temperature” (EDT) in order to obtain a diffusivity value that is representative for the time period of interest (Equation 8). The EDT is a temperature scaled by the Arrhenius function to account for changes in diffusivity over time periods of thermal variability (Christodoulides et al., 1971; Tremblay et al., 2014a):

$$EDT = \frac{-E_a}{R} \left(\ln \left[\frac{1}{t} \int_0^t \exp\left(\frac{-E_a}{RT(t')}\right) dt'_{3He} \right] \right)^{-1} \quad (8)$$

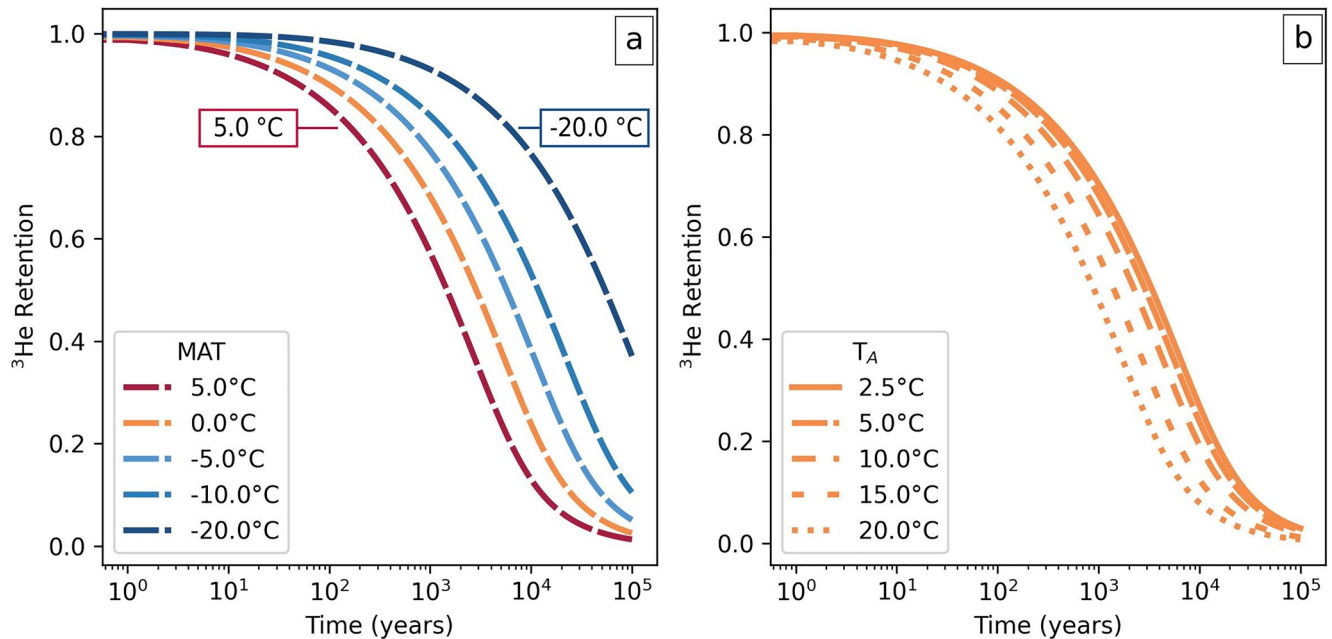


Figure 2. ^3He retention in quartz for a non-eroding surface. The model simulates ^3He retention after exposure at the surface at time 0 starting from an initial concentration of 0.0 atoms g^{-1} . Retention is shown as a function of mean annual temperature (MAT), when keeping the annual temperature amplitude (T_A) equal to 5°C (a) and as a function of seasonal temperature amplitude (T_A), when keeping MAT equal to 0°C (b). Annual temperature cycles are simulated using Equation 11.

Using an EDT allows for the calculation of one diffusivity which integrates over the temperature variations present on daily or seasonal cycles. To improve the model efficiency, we calculated an EDT for every simulated year because it eliminates the need to derive both rock temperature and the ^3He diffusivity ($D(T)$) at sub-annual time steps. In principle, an EDT could also be calculated over longer timescales, as in Tremblay et al. (2014a, 2018), or shorter timescales, depending on the paleoclimatic interval of interest. We refer the reader to Tremblay et al. (2014a) and references therein for a more thorough discussion of the EDT, and its associated sensitivities and uncertainties.

In an open, diffusive system, the total number of atoms that are produced in a grain and the fraction lost by diffusion is only known when compared against a system in which nuclides are completely retained over the timescale of interest. We therefore compare the concentration of ^3He to that of ^{10}Be , scaled for the respective production rates, to yield the proportion of ^3He retention ($R_{3/10}$):

$$R_{3/10} = \left(\frac{C_{3\text{He}}}{C_{10\text{Be}}} \right) \left(\frac{P_{10\text{Be}}}{P_{3\text{He}}} \right) \quad (9)$$

where C_x is concentration of nuclide x (atoms g^{-1}) and P_x is the total surface production rate of nuclide x (atoms $\text{g}^{-1} \text{ yr}^{-1}$). In non-eroding settings and with all other variables (grain size, diffusion kinetics, production rate, etc.) held constant, retention is solely dependent on temperature (Tremblay et al., 2014a, 2014b). Figure 2 indicates the variability in ^3He retention as a function of time and mean annual temperature (MAT) as well as annual temperature amplitude. While the MAT sets the magnitude of the ^3He retention, it is also affected by the annual temperature amplitude.

3. Model Description

3.1. Rationale and Model Setup

Because erosion processes in alpine landscapes are typically stochastic (Ganti et al., 2016; O'Farrell et al., 2009; Sanders et al., 2013), the accumulation and evolution of ^{14}C , ^{10}Be , and ^3He cannot be simulated analytically for most scenarios we seek to evaluate, and therefore must be derived numerically. We thus created a 1D numerical model that simulates the production and loss of CN alongside the bedrock temperature conditions under a variety

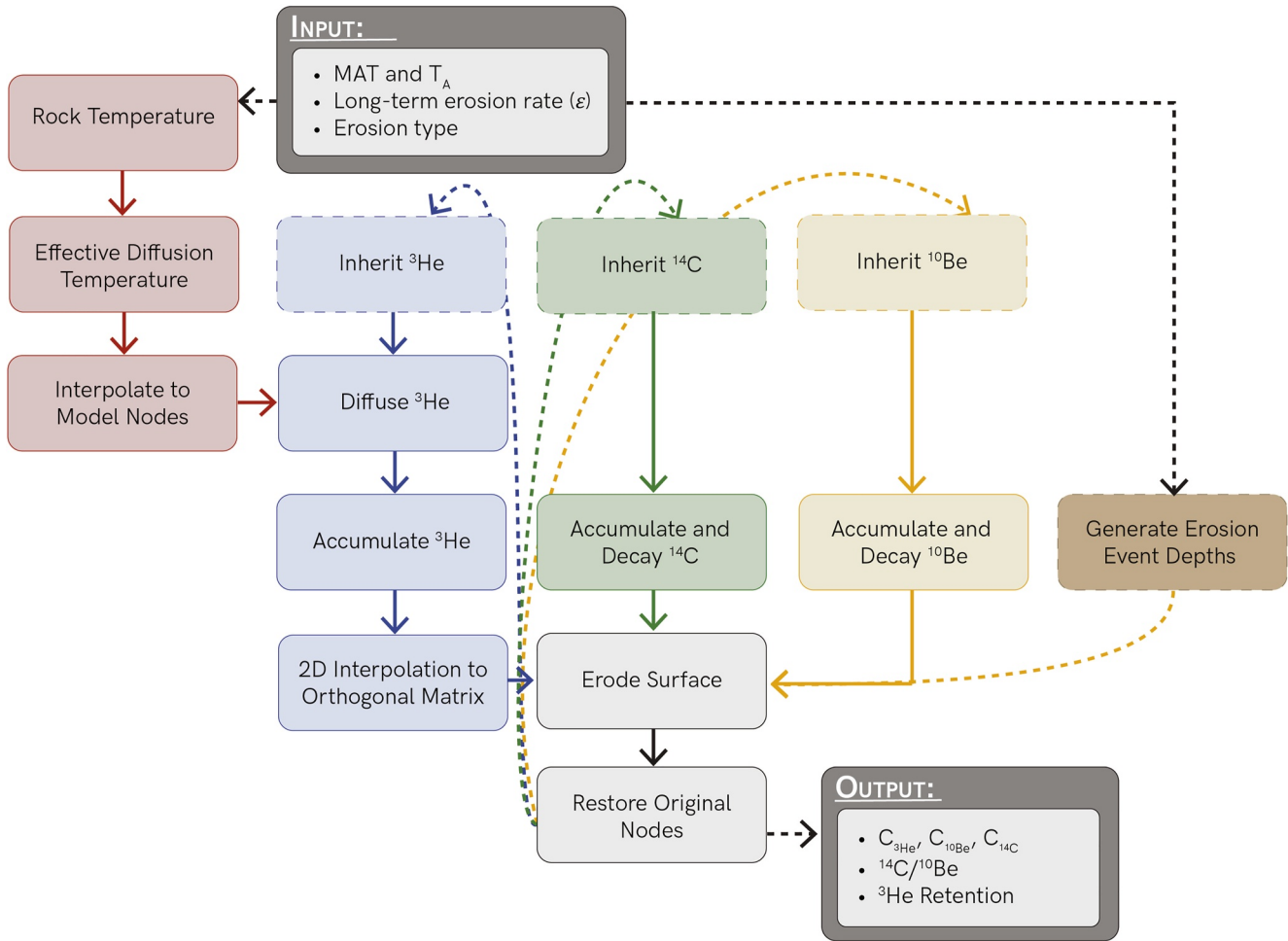


Figure 3. Flow-chart of the numerical model procedure. The model is forced with a surface temperature and an erosion history (“Input” box). During each time step, the model first determines the subsurface temperature conditions and calculates effective diffusion temperatures for all depths. Subsequently, production (^{10}Be , ^{14}C , and ^3He), radioactive decay (^{10}Be , ^{14}C), and diffusion (^3He) of cosmogenic nuclides is calculated. At the end of each time step an erosion event takes place and removes a specific amount of material from the surface to greater depth.

of erosional regimes (Dennis & Scherler, 2022). Model time steps for cosmogenic nuclide production, decay, and diffusion were 1 year. The time step for ground surface temperature was 6 hours. Total simulation duration for stochastic and episodic erosion was 17,500 years, which corresponds roughly with the onset of large-scale glacial retreat in the European Alps following the Last Glacial Maximum (Ivy-Ochs et al., 2008), and 10,000 years for constant erosion. Figure 3 provides a flow chart of the model and Table A1 in Appendix A provides a list of all variables, parameters, and constants.

3.2. Bedrock Temperature

The thermal energy (heat) which is conducted from the surface to depth (we neglect heat flow from below) dictates the diffusivity ($D(T)$) and thereby the retention of ^3He within a quartz grain. If not otherwise indicated, the ground temperatures (T_{z_0}) at the grid node that is closest to the surface are simulated using the equation for sinusoidal temperature variation:

$$T_{z_0}(t) = MAT - T_A \exp\left(-z_0 \sqrt{\frac{\pi}{\alpha P_y}}\right) \cos\left(\frac{2\pi(t)}{P_y} - z_0 \sqrt{\frac{\pi}{\alpha P_y}}\right) \quad (10)$$

where MAT is the MAT (K), T_A is the temperature amplitude of the sinusoidal variation (K), z_0 is the depth of the node nearest to the surface (cm), t is time (s), α the thermal diffusivity of the bedrock ($\text{cm}^2 \text{s}^{-1}$), and P_y the period

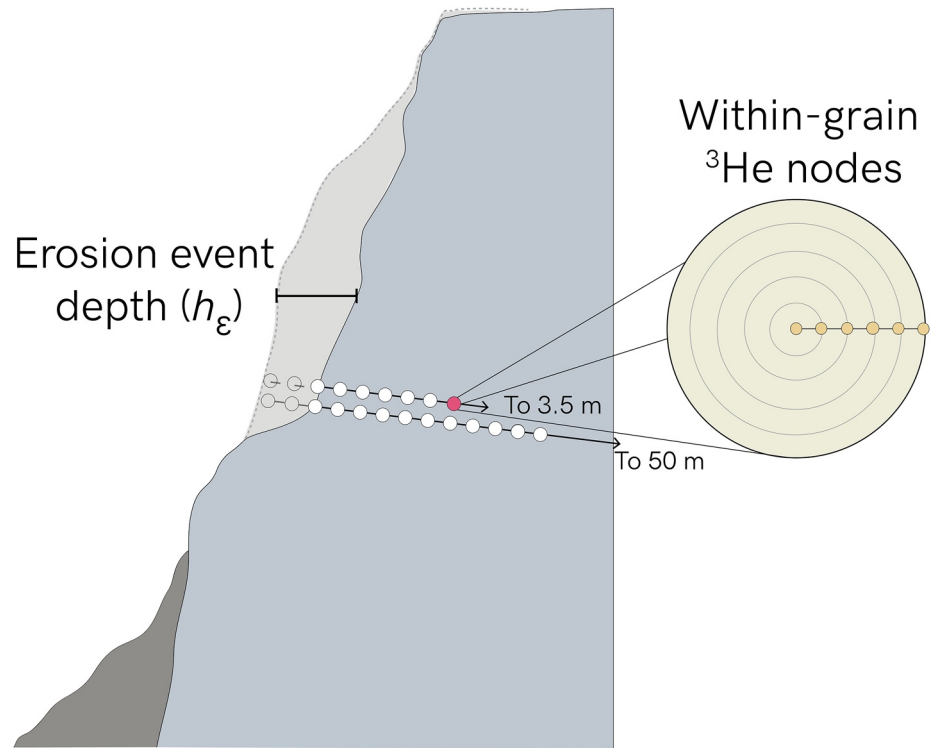


Figure 4. Schematic overview of the 1D model. Nodes are spaced linearly to depth for all nuclides. ^{14}C and ^{10}Be are simulated to 50 m to account for muogenic production, whereas ^3He concentration is solved for only to 3.5 cm. We solve for ^3He concentration within the grain, and the total concentration of the grains at each depth node.

of the sinusoid (Anderson, 1998; Hales & Roering, 2007). Equation 10 yields the analytical solution for the ground temperature at any depth and time, provided a stable surface. However, because we are interested in the thermal evolution of the subsurface as the surface erodes, we could not use Equation 10 to impose the temperature conditions at depth, and instead computed the flux of thermal energy u (W/m^2) using the conduction/diffusion equation (Carslaw & Jaeger, 1959):

$$\frac{\partial u}{\partial t} = \alpha \frac{\partial^2 u}{\partial z^2} \quad (11)$$

Values for the thermal diffusivity of granite reported in the literature vary from $1.34 \times 10^{-2} \text{ cm}^2 \text{ s}^{-1}$ to greater than $1.656 \times 10^{-2} \text{ cm}^2 \text{ s}^{-1}$ (Drury, 1987; Kant et al., 2017), and we chose a thermal diffusivity of the bedrock (α) of $1.52 \times 10^{-2} \text{ cm}^2 \text{ s}^{-1}$ in all experiments. The density of the bedrock (ρ) was set to 2.62 g cm^{-3} .

3.3. ^3He Diffusion in Quartz Grains

Simulating the concentration of ^3He through time under active erosion requires modeling grain-specific production and diffusion at depth (Equations 1–6). Here we follow the approach of Tremblay et al. (2014a) who employed the numerical scheme of Ketcham (2005). Using Ketcham's solution, mineral grains are treated as nested, concentric shells with outer edges defined at nodes equally spaced along the sphere's radius (Figure 4). Diffusion kinetics are computed with respect to the radius, in order to solve for diffusion of ^3He within a grain with the following equation

$$\frac{q_j^{n+1} - q_j^n}{\Delta t} = \frac{D(T)}{2} \frac{(q_{j+1}^{n+1} - 2q_j^{n+1} + q_{j-1}^{n+1}) + (q_{j+1}^n - 2q_j^n + q_{j-1}^n)}{\Delta r^2} + P_j r \quad (12)$$

The solution in Equation 12 employs the common substitution $q = vr$, with v being equal to the number of ^3He atoms and r referring to the radial position within the sphere, and P_j is the ^3He production rate weighted by the

mass of the shell at node j (atoms $\text{g}^{-1} \text{yr}^{-1}$; Ketcham, 2005). Subscript j indicates space and superscript n indicates time. Equation 12 is solved using a Crank-Nicholson scheme. The reader is referred to Ketcham (2005) for a more extensive treatment of the grid setup, boundary node conditions, and the numerical fidelity of this solution.

The concentration of ^3He remaining after production and diffusion is calculated annually, using the depth-dependent EDT at the bedrock nodes. We solve for ^3He concentrations to a maximum depth of 3.5 m and assume a uniform grain diameter of 0.1 cm and a single set of diffusion kinetics (i.e., diffusion in a single domain). Note, however, that multi-domain diffusion models have been found to more accurately reflect ^3He diffusion in some field samples (Tremblay et al., 2014b). In actual field studies, sample-specific diffusion kinetics (for either single or multiple domains) should be used. In all of our experiments the density of quartz was set to 2.65 g cm^{-3} ; activation energy (E_a) was set to 84.5 kJ/mol; and the $\ln(D_0/a)$ was set to 11.1. The average ^3He concentration within a grain is calculated based on the sum of atoms within each shell, relative to the mass of the grain. Because the ^3He nodes represent the bounds of each shell, the number of ^3He atoms at each node is weighted by the shell's spherical volume.

3.4. Production and Decay of ^{10}Be and ^{14}C

Production and decay of ^{10}Be and ^{14}C are computed at each node, to a maximum depth of 50 m using Equations 3 and 4 (Figure 1). Calculating to this maximum depth, while seemingly extreme given the rapid attenuation of cosmogenic nuclide production in the shallow subsurface, ensures accurate representation of muogenic nuclide production. We do not scale nuclide attenuation length scales for inclined surfaces in order to explore broad trends independent of particular slope angles and altitudes, though we again note that this is necessary for interpreting field samples (e.g., DiBiase, 2018; Dunne et al., 1999). We imposed initial concentrations of ^{10}Be and ^{14}C at depth by solving the analytical solution for steady-state erosion given the (imposed) long-term erosion rate (Equation 5). Production rates are those for sea-level high latitude, as reported in Appendix A.

3.5. Parameterization of Erosion

An erosion rate is the amount of material removed during a specific time period, conceptualized here as the depth of an erosion event measured perpendicular to the surface, divided by the timescale of integration, that is, the time step of the model. Because our model is applied in 1D, it is analogous to a rockwall retreat rate. Erosional processes operating in cold environments yield not only erosion rates spanning many orders of magnitude, but also variability in the erosion rate through time. For example, rockfalls can remove meters of material in just a few brief moments, followed by long periods of very little activity. To evaluate the long-term evolution of stochastically eroding landscapes, it is therefore necessary to integrate over a time interval that includes large (rare) events, but does not exaggerate their relative weight. Because we are interested here in the response of landscapes to changes in climate over kyr-timescales, that is, timescales short enough for inferred erosion rates to be skewed by large events, we explored the effects of different erosional regime types (uniform, episodic, and stochastic) on the ^{10}Be -derived erosion rate, the $^{14}\text{C}/^{10}\text{Be}$ ratio, and ^3He retention.

Within our model sequence, erosion occurs annually and is applied prior to nuclide production and decay. The long-term erosion rate, ϵ (cm yr^{-1}), is parameterized under the following three erosion types: (a) a uniform rate applied each time step (uniform erosion); (b) a uniform rate applied at a regular, though not annual, frequency (episodic erosion); and (c) a variable rate wherein the event depths (h_e (cm)) are drawn annually from a Pareto distribution (stochastic erosion).

In the stochastic erosion scenario, event depths are drawn from a generalized Pareto distribution with a mean approximately equivalent ($\pm 10\%$) to the imposed long-term erosion rate. The Pareto distribution and related power law distributions have been shown to accurately reflect the frequency of large stochastic landslides (Stark & Hovius, 2001) and of smaller rockfalls (Dussauge et al., 2003). The probability density function for a generalized Pareto distribution is given as

$$p(x) = c x_m^c x^{-(1+c)} \quad (13)$$

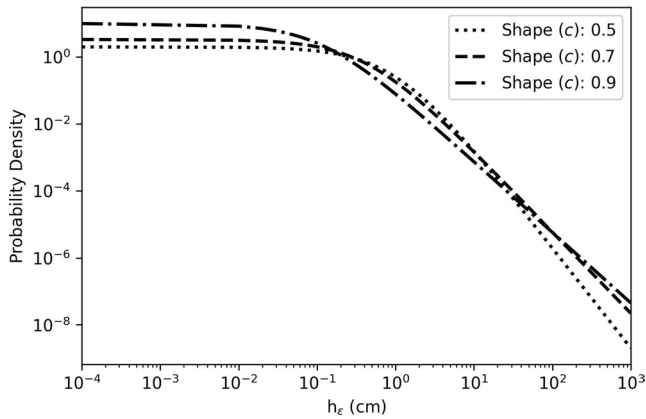


Figure 5. Parametric representation of rockfall size-frequency distribution using a Pareto distribution (Equation 13) and different shape parameter (c) values. The erosion rate for the frequency distributions reported in this figure is 0.1 cm yr^{-1} .

where x_m is the scaling parameter and c is the shape parameter for the distribution (Reiss & Thomas, 1997; Virtanen et al., 2020). Following an erosion event, the depths of the grid nodes are updated by subtracting the eroded amount (h_ϵ):

$$z_{n+1} = \{z_n - h_\epsilon | z_{n+1} \geq 0\} \quad (14)$$

where the subscript n refers to time. Only grid nodes that correspond to non-negative depths are retained. At the end of each time step, the original node depths are restored by linear interpolation from the remaining nodes and depths after the erosion event. Additional nodes (with concentrations of 0.0 atoms g^{-1}) are added to the bottom of the rock column to replace those removed during erosion. Probability density functions of three different Pareto distributions scaled to yield a long-term erosion rate (ϵ) of approximately 0.1 cm yr^{-1} are shown in Figure 5.

3.6. Boundary Conditions

3.6.1. Surface Erosion

We conducted erosion experiments categorized under three types of erosion: uniform erosion, episodic erosion, and stochastic erosion. These erosion types were defined in order to cover a range of erosional dynamics for temperature-dependent weathering mechanisms in high-alpine settings. Cosmogenic nuclide concentrations were evaluated under uniform erosion rates of $0.01, 0.075, 0.1, 0.125,$ and 1.0 cm yr^{-1} . Likewise, nuclide concentrations under episodic erosion at rates of $0.05, 0.1, 0.25 \text{ cm yr}^{-1}$ were evaluated with erosion event recurrence frequencies of 100 and 1,000 years. Experiments with stochastic erosion were evaluated using erosion event depths drawn from a Pareto distribution, first with differing long-term erosion rates, and then with variable shape parameter values (c) (Figure 5). The long-term erosion rates correspond to the mean of the Pareto distribution, scaled by a factor x_m (Equation 13) in order to return a mean within 10% of the input erosion rate. For the simulations with variable erosion rates, the erosion rates are $0.05, 0.1,$ and 0.25 cm yr^{-1} and the Pareto shape value was 0.7. For the shape value tests, c was set to 0.5, 0.7, and 0.9, and the erosion rate was 0.1 cm yr^{-1} . Table B1 in Appendix B reports the parameters which were varied for each model run, and the relevant figure.

3.6.2. Bedrock Surface Temperature

The forcing of bedrock surface temperatures varied by erosion type. We evaluated the relative retention of different temperature regimes only under uniform erosion, in order to distinguish between erosion-type-induced and environmental-temperature-induced differences in retention. Under uniform erosion, experiments were conducted at five different MATs, ranging from -20°C to 5°C . The annual temperature amplitude (T_A) in these experiments (Figure 2a) was 5°C . We additionally tested the effect of variable temperature amplitudes, shown in Figure 2b. These experiments were forced using a MAT of 0°C . For experiments employing non-uniform erosion, the MAT was set to 0°C and the T_A was set to 5°C .

3.7. Model Evaluation

In this study, we focus on samples collected from the bedrock surface only, although depth profiles (e.g., Mair et al., 2019) could be obtained from the model results. Based on the expectation that most bedrock surfaces erode by discrete rockfalls, which commonly occur over meter-to tens of meter-scale lateral extents (Legay et al., 2021), we employ a sampling scheme in which many singular rock chips of equal size are collected over a larger area and combined (amalgamated) into one sample in order to more accurately approximate the true erosion rate (e.g., Sarr et al., 2019; Small et al., 1997; Ward & Anderson, 2011). To imitate 2D surface sampling in our 1D model, we rely on “time for space substitution” and sampled rock chips from each simulation at random years without replacement. Each rock chip corresponds to one “sub-sample” within a larger “amalgamated sample,” and is assigned a thickness of 5 cm. The default number of sub-samples within an amalgamated sample is 30, unless otherwise specified. In practical terms, this means we are simply taking the average of 30 randomly selected

Table 1
Terminology Used Within the Text

Term	Description
Annual erosion rate	The erosion rate over a 1-year interval;
Long-term erosion rate	The erosion rate calculated by dividing the total material eroded following model spin-up by the total time elapsed following spin-up;
¹⁰ Be-derived erosion rate	The apparent erosion rate calculated from the mean ¹⁰ Be concentration of an amalgamated sample;
Observed ¹⁴ C/ ¹⁰ Be ratio	The ¹⁴ C/ ¹⁰ Be ratio returned from a sampled model scenario;
Expected ¹⁴ C/ ¹⁰ Be ratio	The ¹⁴ C/ ¹⁰ Be ratio expected under uniform, steady state erosion, given the ¹⁰ Be-derived erosion rate;
Observed ³ He retention	The ³ He retention returned from a sampled model scenario;
Expected ³ He retention	The ³ He retention expected under uniform, steady state erosion, given the ¹⁰ Be-derived erosion rate;

surface concentrations. These samples were selected after achieving true (uniform erosion) or quasi (episodic and stochastic) steady-state, no earlier than model year 1750. For each amalgamated sample, we calculated an erosion rate from the average ¹⁰Be concentration, the percent retention from the average ³He concentration, and the average ¹⁴C/¹⁰Be ratio. The sampling procedure was repeated 1,000 times for each scenario in order to obtain a larger statistical sample from each model run. Because we have imposed a uniform thermal history for our scenarios and are interested in whether erosion style, rather than the thermal history, affect ³He interpretations, we report our data as ³He retentions.

In order to avoid confusion with respect to terminology throughout the following chapters, we differentiate between the various, related model inputs and outputs using the terminology listed in Table 1. These terms are intended to clarify the calculations or outputs, which may be closely related. The “annual erosion rate” and “long-term erosion rate” are both calculated using absolute amounts of eroded material, though the long-term erosion rate integrates over all time post spin-up, whereas the annual erosion rate integrates over 1 year only, and, in the case of stochastic erosion, corresponds to the erosion event depth (h_e). Both are inputs imposed on the model. In contrast, “¹⁰Be-derived erosion rates” are apparent erosion rates calculated from the ¹⁰Be concentrations returned by the model according to the sampling procedure outlined above. Similarly, the “observed ¹⁴C/¹⁰Be ratio” refers to ¹⁴C/¹⁰Be calculated from the mean concentrations of all sub-samples. This is in contrast to the “expected ¹⁴C/¹⁰Be ratio”, which is the ratio expected for uniform, steady-state erosion given the apparent ¹⁰Be-derived erosion rate (Figure 1c). “Observed ³He retention”, like the observed ¹⁴C/¹⁰Be ratio, is calculated from the all sub-sample mean ³He concentration divided by the all sub-sample mean ¹⁰Be concentration, scaled by the production rates (Equation 9).

4. Model Results

4.1. Uniform Erosion Rate Scenarios

Under uniform erosion, the surface concentration of both ¹⁴C and ¹⁰Be depends, as expected, on the imposed long-term erosion rate. Likewise, ³He concentrations are, to a first-order, set by the imposed long-term erosion rates (Figure 6). But unlike ¹⁰Be and ¹⁴C, ³He surface concentrations and retentions are modulated by both the continuous removal of helium-rich material from the surface and the environmental temperature (Tremblay et al., 2014a). ³He surface concentrations therefore approach dynamic equilibrium more rapidly in actively eroding compared to non-eroding settings (Figure 6). At very high erosion rates (1.0 cm yr⁻¹), ³He concentrations are quite low, but retention is high (near 90%) as rapid erosion limits the time for diffusive loss. As erosion rates approach zero, ³He concentrations increase, while the overall percentage of ³He retained decreases, as ³He diffuses out of the grain (Figure 6). Erosion rate magnitude therefore exerts an additional, important control on observed ³He retention, alongside temperature.

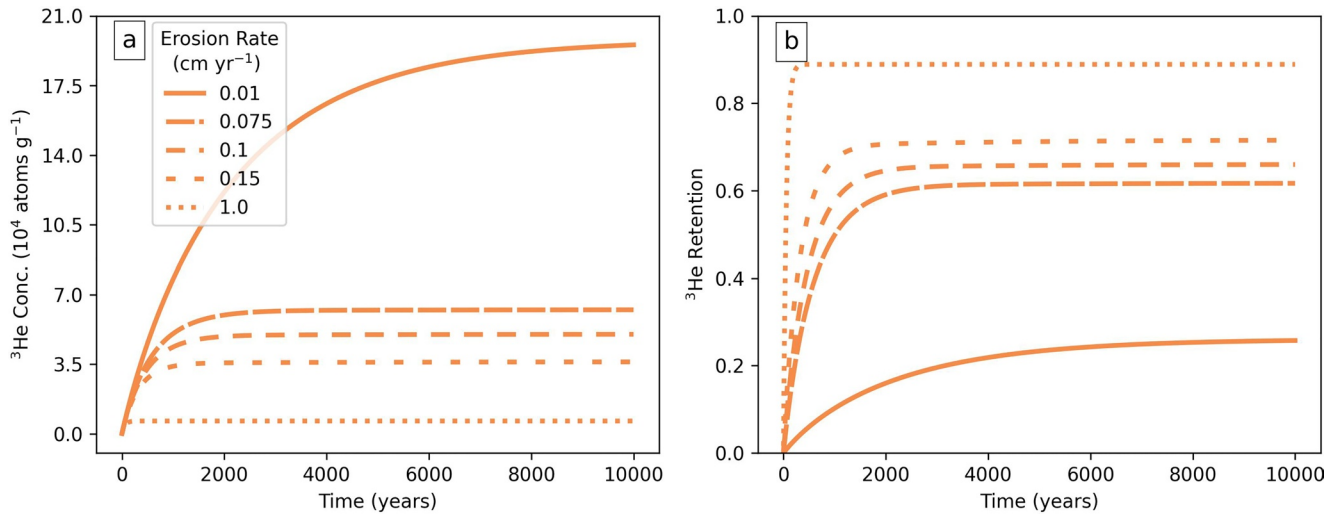


Figure 6. Surface ^3He concentrations (a) and retention (b) under uniform erosion for a range of erosion rates.

4.2. Episodic Erosion Scenarios

In contrast to the uniform erosion rate scenarios, wherein surface concentrations are relatively stable from year to year, surfaces that undergo episodic erosion have ^{14}C and ^{10}Be surface concentrations that fluctuate with time (cf., Small et al., 1997). The differences between the actual and the long-term average ^{14}C and ^{10}Be surface concentrations are dictated by the recurrence frequency of rockfalls and their magnitudes. Figure 7 shows the ^{10}Be -derived erosion rate error, as compared to the long-term erosion rate, for three scenarios, each with 100-year- and 1,000-year-recurrence frequencies. At 1,000-year intervals, the erosion rate is more likely to be underestimated by our sampling strategy (Figure 7). This effect was particularly pronounced at the high erosion rate (0.25 cm yr^{-1}). The observed $^{14}\text{C}/^{10}\text{Be}$ ratio under episodic erosion closely follows the expected ratio, except at the highest erosion rate (0.25 cm yr^{-1}), and particularly at the high recurrence frequency of 1,000 years, where the $^{14}\text{C}/^{10}\text{Be}$

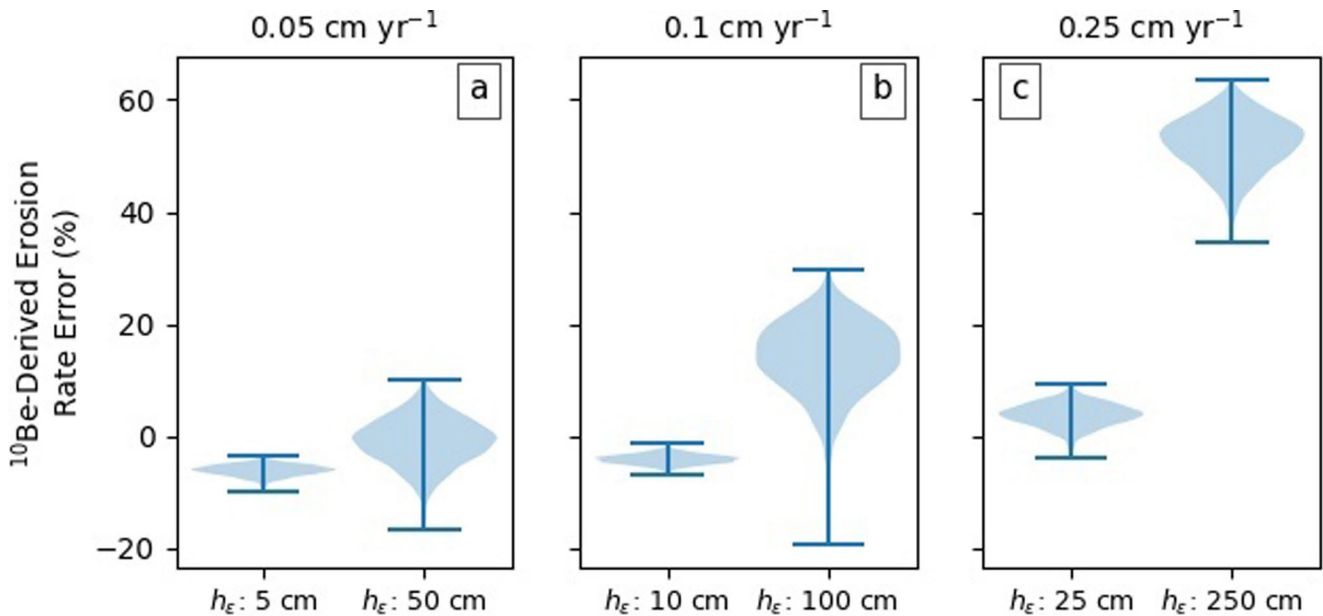


Figure 7. ^{10}Be -derived erosion rate error under episodic erosion, for long-term erosion rates of 0.05 cm yr^{-1} (a), 0.1 cm yr^{-1} (b), and 0.25 cm yr^{-1} (c). In each panel, the erosion event depths (h_ϵ) are set to values that yield the long-term erosion rate for recurrence frequencies of 100 (left) and 1,000 (right) years. Negative error indicates overestimation of the long-term erosion rate, whereas positive error indicates underestimation.

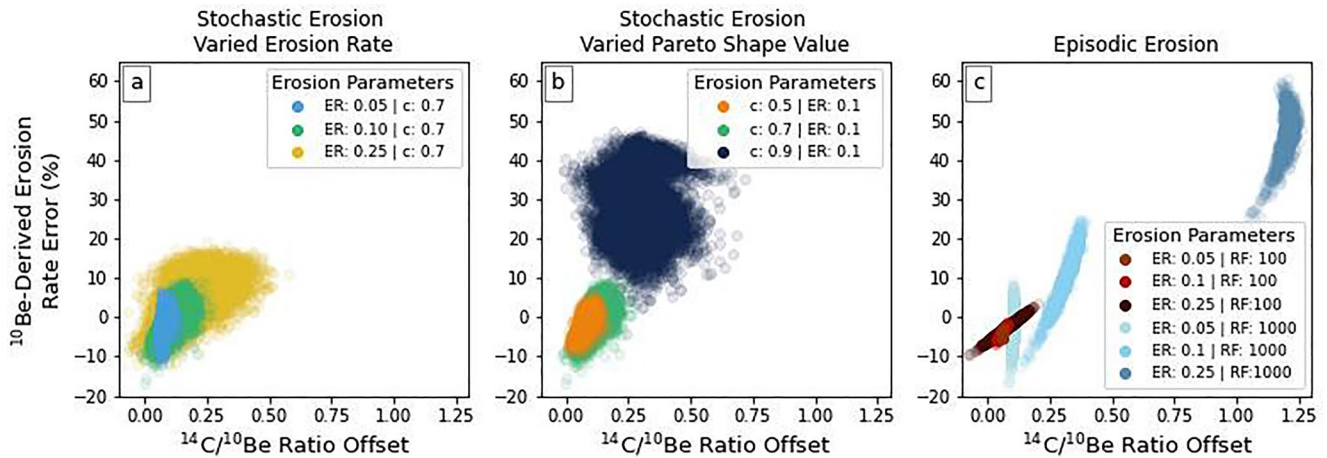


Figure 8. ^{10}Be -derived erosion rate error (%) as a function of the $^{14}\text{C}/^{10}\text{Be}$ ratio offset. (a) Stochastic erosion with different erosion rates (ER) of 0.05, 0.1, and 0.25 cm yr^{-1} and constant shape parameter ($c = 0.7$); (b) Stochastic erosion with different c and constant ER of 0.1 cm yr^{-1} ; (c) Episodic erosion with differing ERs of 0.05, 0.1, and 0.25 cm yr^{-1} and recurrence frequencies (RF) of 100 and 1,000 years. Note that for the RF of 100 years, the data points for the differing ER plot on top of each other.

ratio mirrors the magnitude of the offset between the measured erosion rate and the long-term erosion rate (Figure 8c). The retention of ^3He is not significantly altered under any of the episodic erosion scenarios.

4.3. Stochastic Erosion Scenarios

Stochastic erosion differs from the episodic erosion in that the magnitude of erosion events varies from year to year (see chapter 3.5 as well as Table B1). We used our model to explore the effect that (a) different long-term erosion rates, and (b) different shape parameter values of the Pareto distribution have on CN concentrations and derived measurements. The spread of the error of the ^{10}Be -derived erosion rate increases at higher erosion rates and shape parameter values (Figures 8a and 8b). Likewise, the offset in the $^{14}\text{C}/^{10}\text{Be}$ ratio increases with the error of the ^{10}Be -derived erosion rate (Figures 8a and 8b). Stochastic erosion simulations indicate strongly variable CN concentrations through time (Figure 9). As the system evolves, the CN concentrations fluctuate about a concentration which corresponds to that expected for uniform erosion at the ^{10}Be -derived erosion rate, though the concentrations are often higher than this value (Figure 9). ^{10}Be -derived erosion rates inferred from randomly selected, amalgamated surface samples therefore generally underestimate the long-term erosion rate (Figure 10). The magnitude of this underestimation increases at higher erosion rates (Figure 10). Unlike erosion rates, sample-based ^3He retention for stochastic erosion closely approximates that expected for the corresponding ^{10}Be -derived erosion rate (Figure 10).

The magnitude of the ^{10}Be -derived erosion rate error depends on the shape parameter value c of the Pareto distribution. Recall that the shape value dictates the “stochasticity” of erosion events: as it approaches zero, the frequency of small events increases while the likelihood of large events decreases. Consequently more of the erosion is taken up by the largest events when the shape parameter value is high and the erosion event depths are less-equally distributed. This is reflected in ^{10}Be -derived erosion rates, which are offset from the long-term erosion rate by up to approximately 45% under the most stochastic models (Figure 11c). While the mean of measured ^3He retention values is still close to the expected value for most models, the range of observed error is notably wider under increasingly stochastic models (Figure 11).

5. Discussion

5.1. Inferring Erosion Rates and Mechanisms With ^{10}Be and ^{14}C

5.1.1. Non-Uniform Erosion Leads to Differences Between Long-Term and ^{10}Be -Derived Erosion Rates

Erosion rates calculated from ^{10}Be concentrations are usually inferred from the absolute concentration of ^{10}Be in a sample relative to the site-specific production rate, and assuming uniform (steady-state) erosion (Equation 5).

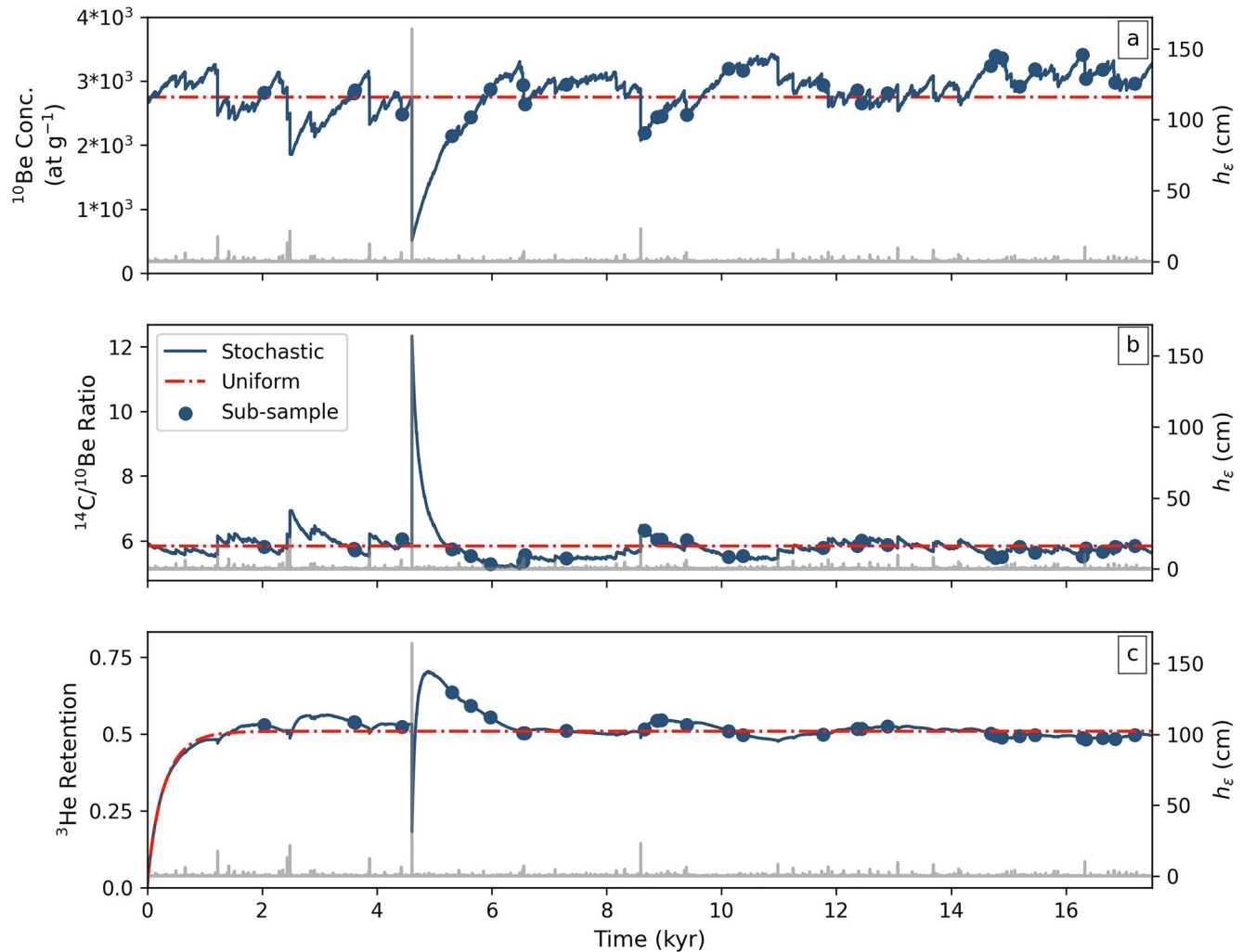


Figure 9. Example of the surface evolution of CN parameters under stochastic erosion scenario. ^{10}Be concentration (a), $^{14}\text{C}/^{10}\text{Be}$ (b), ^3He retention (c) are shown versus time. Erosion events (rockfalls) are shown as gray bars which correspond to the erosion event depth scale (h_e) on the right-hand y-axis. Circular markers represent individual sub-samples taken as part of an amalgamated sample. The red line indicates values expected under uniform erosion for the ^{10}Be -derived erosion rate of this scenario. The Pareto shape parameter value in this scenario is 0.9, the long-term erosion rate is 0.1 cm yr^{-1} , the mean annual temperature is 0.0°C and the T_A is 5.0°C .

Concentrations from samples which have undergone non-uniform erosion therefore do not satisfy the assumption of steady-state, and are subject to uncertainty (e.g., Small et al., 1997). Our results show that under the amalgamated sampling regime described above, erosion rates are likely to be underestimated in non-uniformly eroding environments when inferred from ^{10}Be concentrations alone (Figures 7, 10 and 11).

Consider the case of episodic erosion. At the lowest erosion rate (0.05 cm yr^{-1}), the magnitude of the error on the inferred ^{10}Be -derived erosion rate and the long-term erosion rate is small, nearly negligible regardless of the rockfall recurrence frequency (Figure 7a). At higher erosion rates, however, both the variability in the ^{10}Be -derived erosion rates and the error of the ^{10}Be -derived erosion rate increase, though the magnitude of the error is dependent on the recurrence frequency of the erosion event (Figures 7b and 7c). This occurs, in part, because our sampling strategy over-represents the stasis period between erosion events and the correspondingly higher ^{10}Be concentrations. In scenarios with high recurrence-frequencies and shallow erosion event depths (h_e), the surface concentration of ^{10}Be never strongly deviates from the concentration expected under uniform erosion. But as the recurrence interval, and therefore the time between erosion events, increases, surface concentrations of ^{10}Be are considerably higher than those expected under uniform erosion, and because of the low recurrence frequency, the likelihood of sampling one of these high-concentration years is high. Thus, at 100-year recurrence frequencies, ^{10}Be -derived erosion rates closely approximate the long-term erosion rate, whereas at 1,000-year recurrence

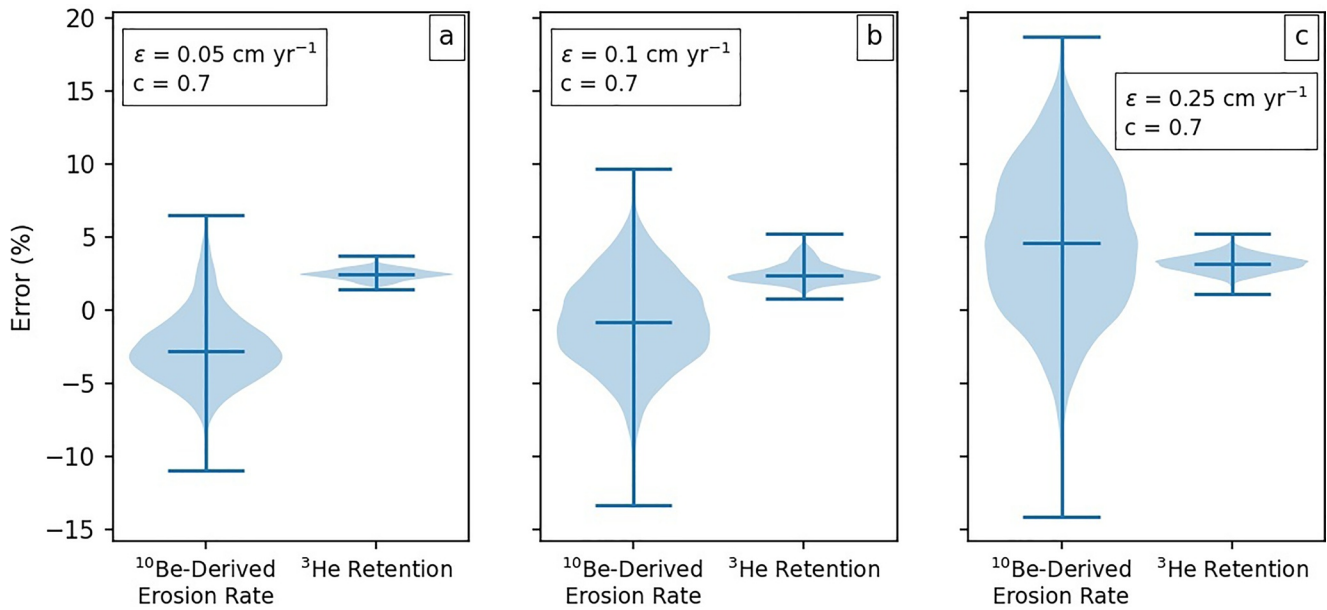


Figure 10. ^{10}Be -derived erosion rate and ^3He retention errors under stochastic erosion for long-term erosion rates of 0.05 cm yr^{-1} (a), 0.1 cm yr^{-1} (b), and 0.25 cm yr^{-1} (c). The shape parameter value for all three scenarios is 0.7. Negative error corresponds to overestimation while positive error indicates underestimation. The center lines correspond to the mean error of the entire sample set and the maximum and minimum lines correspond to the extrema. We do not identify or exclude outliers. Each violin plot presents data from 10,000 random amalgamated samples.

frequencies, the ^{10}Be -derived erosion rates are underestimated by as much as 60%, in the case of 0.25 cm yr^{-1} (Figure 7c).

Our results therefore demonstrate that amalgamated samples from steep hillslopes in rather rapidly eroding environments ($>0.05\text{ cm yr}^{-1}$) likely yield minimum erosion rates. Small et al. (1997) used a similar finite-difference scheme to evaluate the effect of episodic erosion via “chips” (erosion event depths) up to 1 m. They found that episodic bedrock erosion rates estimated using individual chips from the surface frequently yielded incorrect

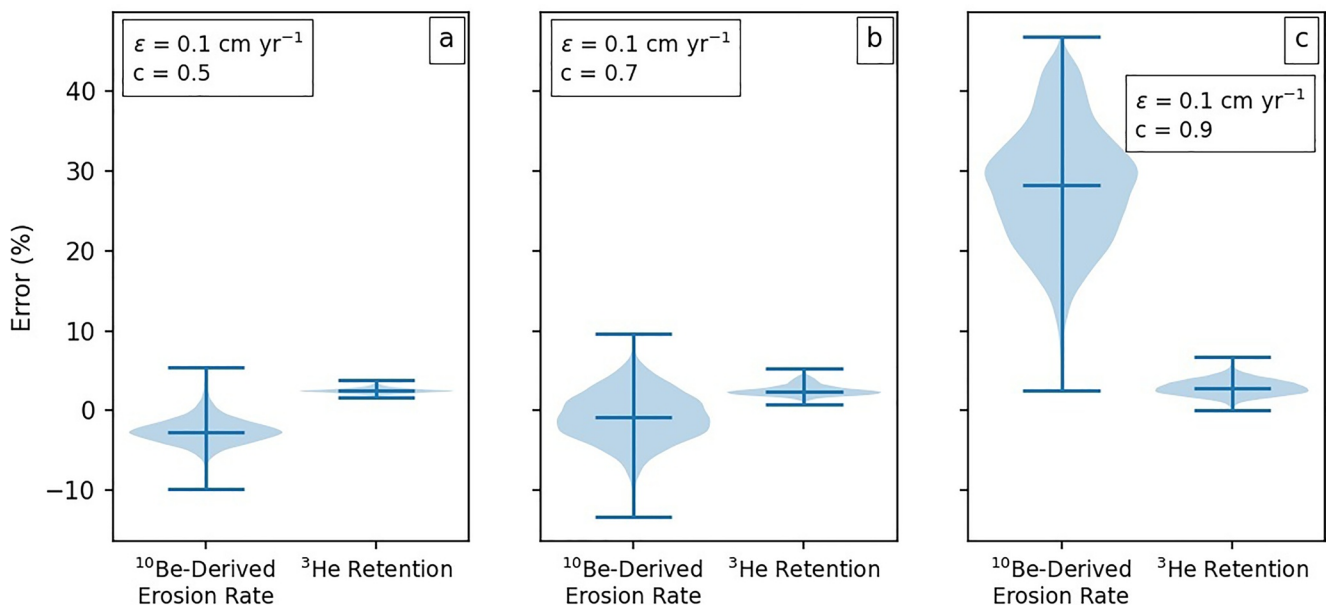


Figure 11. ^{10}Be -derived erosion rate and ^3He retention errors under stochastic erosion for different shape parameter values of 0.5 (a), 0.7 (b), and 0.9 (c). The long-term erosion rate for all three scenarios is 0.1 cm yr^{-1} . Negative error corresponds to overestimation while positive error indicates underestimation.

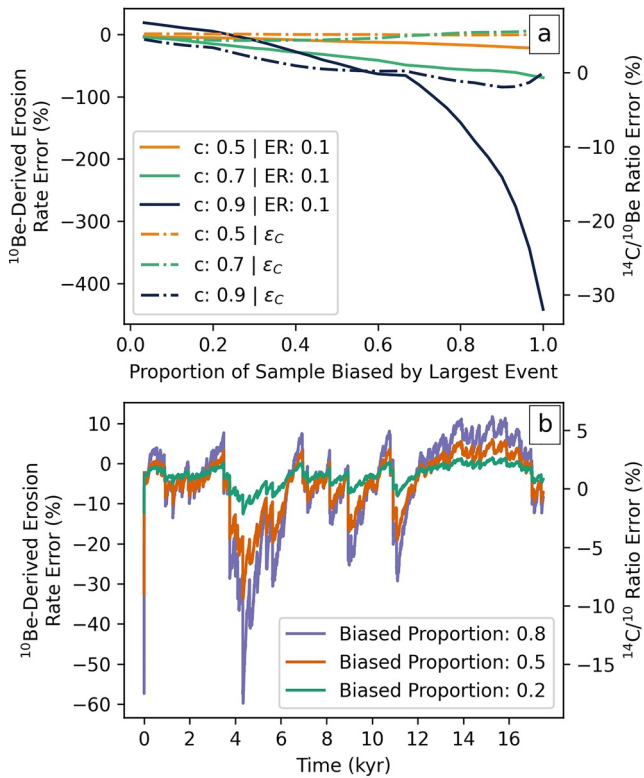


Figure 12. Biasing amalgamated samples with surface concentrations under stochastic erosion. The ^{10}Be -derived erosion rate error and $^{14}\text{C}/^{10}\text{Be}$ ratio error are reported after biasing with concentrations following the largest erosion event (a) and with the surface concentration of the given year at variable weight proportions (b). Erosion rates are reported in cm yr^{-1} . ϵ_c indicates a corrected erosion rate, as discussed in Section 5.1.3, calculated using Equation 15 with the coefficients given in Table A1. Positive error indicates underestimation of the long-term erosion rate by the ^{10}Be -derived erosion rate and negative error indicates overestimation.

Small et al., 1997). This sampling procedure assumes that (a) rockfalls across a surface are heterogeneous with respect to space and (b) that an amalgamated sample collected from a surface was not biased by one or several erosion events. Nevertheless, if there exist causal links, such as accumulated rock damage due to frost weathering processes (Matsuoka, 2019) or other rockfall triggers (such as extended periods of warm temperatures), several large rockfalls distributed across the surface of the rockwall may occur in rapid succession, and our assumptions for sample amalgamation are no longer valid. Furthermore, collecting random samples in steep, bedrock hillslopes is challenging, and sampling strategies must consider a hillslope's accessibility, which may not allow for access to the entire hillslope. Higher-density sampling of more easily accessible portions of a hillslope can likewise lead to inadvertent biasing by one or several events. In order to explore the sensitivity of amalgamated samples to biasing by single events, we simulated samples that are dominated by the largest erosion event (i.e., the maximum possible bias for the simulation) at prescribed “weights”, and we call these samples “weighted amalgamated samples” (Figure 12).

When deliberately incorporating material from a surface immediately after the deepest erosion event (Figure 12a), the resulting bias on erosion rates is negligible under the least stochastic scenario ($c = 0.5$), and under all scenarios when the proportion of the whole sample is not weighted by more than appx. 40% with large-event subsamples (Figure 12a). Weighting an amalgamated sample by the concentration of any individual year (which is not influenced by a recent large event) is likewise negligible, as is seen in the time interval between 12.5 and 17.5 kyr in Figure 12b. Nevertheless, as the weight of the selected subsample increases with respect to the whole sample, so too does the magnitude of the bias in the ^{10}Be -derived erosion rate (Figures 12a and 12b). Alongside the bias in

erosion rate estimates, while pointing to the fact that amalgamation of many chips should yield an accurate mean erosion rate. They additionally highlight that the errors in erosion rate estimates for samples containing large chip sizes that spall infrequently are correspondingly higher. These results broadly agree with our study, though we note that our maximum erosion event depth (analogous to their “chip size”) is 250 cm, and our maximum erosion rate errors are therefore much larger than those suggested by their study.

Though episodic erosion is straightforward to conceptualize, records of rock-fall events suggest that the distribution of event sizes in high-mountain areas is more robustly described by Pareto distributions (Dussauge et al., 2003; Stark & Hovius, 2001; Wood et al., 2015). Our data demonstrate the effect of distribution shape (i.e., stochasticity), on ^{10}Be -derived erosion rates inferred from rockwalls undergoing stochastic erosion. Under stochastic erosion scenarios, higher shape parameter values yield larger differences between the long-term erosion rate and the ^{10}Be -derived erosion rate (Figure 11), consistent with the findings of Muzikar (2019). Like in episodic erosion scenarios with longer recurrence frequencies, the stochastic erosion scenarios with high shape parameter values reflect surfaces where large erosion events exist, but they are rare (Figure 9). These large events account for a non-trivial part (up to 60%) of the total erosion occurring in a model run. Therefore, under a random sampling setup, the likelihood of randomly sampling the surface after a large event, when concentrations are far below those expected for uniform erosion, is low, whereas the likelihood of sampling a surface with a higher concentration is high. Amalgamated samples thus have higher concentrations overall, and correspondingly lower ^{10}Be -derived erosion rates. Like in episodic erosion, we find that ^{10}Be -derived erosion rates are likely minimum erosion rates if the sampling conditions we impose here are replicated in the field.

5.1.2. Non-Random Sampling Can Lead to Biased Inferred Erosion Rates

So far, we have assumed that erosion rates inferred from amalgamated samples randomly collected across a stochastically eroding surface better represent the long-term average erosion rate than singular, point-based samples (cf.,

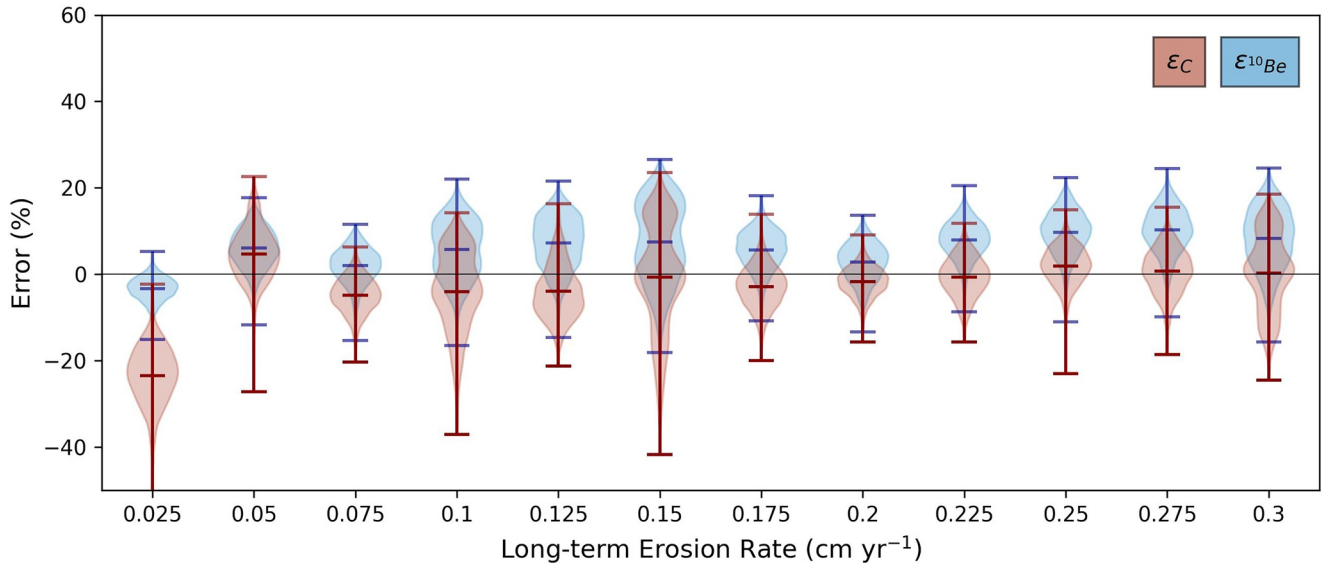


Figure 13. Error of the corrected erosion rate (ϵ_c) and the ^{10}Be -derived erosion rate ($\epsilon_{10\text{Be}}$) for the correction test data set. The shape parameter value for all simulations in the correction test dataset is 0.8.

the ^{10}Be -derived erosion rate, the $^{14}\text{C}/^{10}\text{Be}$ ratio likewise increases compared to the value expected for the measured steady-state erosion rate for the whole amalgamated sample (Figures 12a and 12b). It is therefore possible to identify a biased amalgamated sample by comparing the concentration of ^{14}C against ^{10}Be . As mentioned above, the offset in the observed $^{14}\text{C}/^{10}\text{Be}$ ratio versus that expected under uniform erosion reflects the depth from which the surface sample was exhumed. Therefore, an observed $^{14}\text{C}/^{10}\text{Be}$ ratio that is higher than the ratio which is expected under uniform erosion, indicates a deeper excavation depth for recent erosion events.

5.1.3. Deriving Representative Long-Term Erosion Rates Using ^{10}Be and ^{14}C

Differences between the ^{10}Be -derived erosion rate and the long-term erosion rate that result both from erosion style and from biasing an amalgamated sample, can be identified using a corresponding error in the expected versus observed $^{14}\text{C}/^{10}\text{Be}$ ratio (Figures 12a and 12b). The basis for this identification is the fact that the ratio of ^{14}C to ^{10}Be is not uniform with depth, due to the higher contribution of muons to the total ^{14}C production (Figure 1). The surface ratio of $^{14}\text{C}/^{10}\text{Be}$ therefore represents the depth from which material has been excavated following an erosion event. Deviation from the expected surface $^{14}\text{C}/^{10}\text{Be}$ ratio under uniform erosion rates (Figure 1b) therefore reflects perturbations to uniform erosion. The magnitude of the $^{14}\text{C}/^{10}\text{Be}$ ratio offset scales with the magnitude of the error on the ^{10}Be -derived erosion rate compared to the long-term erosion rate (Figure 8).

We tested whether the offset between the expected surface $^{14}\text{C}/^{10}\text{Be}$ ratio under uniform erosion, $\left(\frac{C_{14\text{C}}}{C_{10\text{Be}}}\right)_{UE}$, the observed $^{14}\text{C}/^{10}\text{Be}$ ratio, $\left(\frac{C_{14\text{C}}}{C_{10\text{Be}}}\right)_{OBS}$, and the ^{10}Be -derived erosion rate, $\epsilon_{10\text{Be}}$, can serve as a meaningful predictor of the ^{10}Be -derived erosion rate error (cm yr $^{-1}$) by fitting a multivariate linear regression to the variable erosion rate and variable Pareto shape value datasets using the LinearRegression function of the Python scikit-learn package (Figures 10 and 11; Pedregosa et al., 2011). Adding this approximated error to the ^{10}Be -derived erosion rate returns a “corrected” erosion rate:

$$\epsilon_c = \left[M_1 \left(\frac{C_{14\text{C}}}{C_{10\text{Be}}} \right)_{OBS} + M_2 (\epsilon_{10\text{Be}}) + M_3 \left(\left(\frac{C_{14\text{C}}}{C_{10\text{Be}}} \right)_{OBS} - \left(\frac{C_{14\text{C}}}{C_{10\text{Be}}} \right)_{UE} \right) \right] + \epsilon_{10\text{Be}} \quad (15)$$

where ϵ_c is the corrected erosion rate. The coefficients $M_{1,3}$ will vary as a function of the surface $^{10}\text{Be}/^{14}\text{C}$ ratio and are therefore dependent on the site-specific production rates for both nuclides. The values of the coefficients used for the corrections shown in Figures 12 and 13 are reported in Table A1.

After calculating our regression terms from the training dataset, we tested the linear model on a new dataset of 24 stochastic-type scenarios, all with a common Pareto distribution shape value of 0.8, and erosion rates varying from 0.025 cm yr^{-1} to 0.3 cm yr^{-1} . The shape value of 0.8 was chosen so as not to correspond with the shape values in the training data set. Using Equation 15, we corrected the ^{10}Be -derived erosion rates and compared them against the long-term erosion rates and the original ^{10}Be -derived erosion rates (Figure 13). The erosion rate correction is best applied to erosion rates which fall within the range of the training data set (0.05 cm yr^{-1} – 0.25 cm yr^{-1}). Outside of this range, the error of the corrected erosion rates is not lower than that of the ^{10}Be -derived erosion rates. Within the bounds of the training data set erosion rates (0.05 – 0.25 cm yr^{-1}), the corrected erosion rates are nearly always better at approximating the long-term erosion rate than the ^{10}Be -derived erosion rate alone (Figure 13). Likewise, biased samples which disproportionately represent a large event can also be corrected using Equation 15, reducing the error of the ^{10}Be -derived erosion rate of biased samples (Figure 12).

Equation 15 is a useful predictor of the long-term erosion rate because each variable in the regression relates to a physical parameter of an eroding rock column. Profiles of cosmogenic nuclide concentrations taken perpendicular to a surface reflect both the nuclide production mechanisms as well as the erosional history of the surface (Braucher et al., 2009; Hidy et al., 2010; Mair et al., 2019). Uniform, steady-state erosion not only yields constant, calculable surface concentrations, but also an expected profile shape with known concentrations below the surface (Figure 1b). Therefore, in a surface which has recently lost considerable material due to a large, stochastic erosion event, a sample's $^{14}\text{C}/^{10}\text{Be}$ ratio corresponds to its former depth prior to exposure, and the ^{10}Be -derived erosion rate (or ^{10}Be concentration) corresponds to the concentration expected at that depth for the long-term erosion rate prior to the rockfall. The multivariate linear regression model therefore relates the depth at which the sample sat prior to a rockfall (from the $^{14}\text{C}/^{10}\text{Be}$ ratio) to the pre-rockfall long-term erosion rate (from the ^{10}Be concentration). The correction is particularly useful for what we call “biased” samples (Figure 12), because more material in the amalgamated sample is derived from one particular depth, and the signature of this event is not dampened via amalgamation. Finally, we note that our terminology suggests the calculated erosion rates are themselves “correct”; but they are correct only inasmuch as they more accurately represent an integration timescale that incorporates, but does not over- or under-emphasize, the contribution of large stochastic events.

5.2. Evaluating Thermal Histories Using ^3He and ^{10}Be

5.2.1. Erosion Style Does Not Affect ^3He Retention

With all other factors held constant, the concentration of ^3He retained relative to a nuclide which is not diffusively lost (in this case, ^{10}Be) reflects a sample's integrated thermal history during exposure to cosmic rays (Tremblay et al., 2014a, 2018). In order to make quantitative inferences for eroding surfaces, total ^3He retention must either not be altered by erosion, or be altered in a predictable way, in samples which have experienced the same thermal history. Our modeled data suggest a sensitivity of ^3He retention to erosion rate, but an insensitivity to erosion type, indicating its straightforward use as a paleothermometer even in stochastically eroding landscapes.

Uniform erosion dictates the initial magnitude of ^3He retention in quartz (Figure 6) and should be accounted for in paleothermometric interpretations. Under the most stochastic scenarios, where up to 60% of total erosion occurs via several high-magnitude events, measured ^3He retentions are slightly offset from the retention expected under uniform erosion, with differences in measured versus expected retention of up to 5% (Figures 10 and 11). For a wrongly assumed stable surface that experienced no change in MAT or T_A , maximum retention differences of appx. 5% correspond to inferred MAT differences of 2.5 – 5°C (Figure 2). Under less stochastic scenarios, and lower erosion rates, retention more closely matches that expected under constant erosion (Figures 10a and 11a), though still with some slight offset, up to 4%.

Given that erosion rates inferred from ^{10}Be concentrations vary in their fidelity to the long-term erosion rate, depending on the shape (“stochasticity”) of the rockfall distribution (Figure 11), it may be initially surprising that ^3He retentions are not likewise offset. But recall that ^3He retention is determined by scaling the ratio of ^3He and ^{10}Be concentrations by the surface production rates to yield one value which summarizes the total amount of ^3He retained versus the amount which was produced (Equation 8). Because muogenic production rates of ^3He in quartz are poorly constrained, and herein assumed to be negligible (cf., Tremblay et al., 2014a, 2018), all production occurs via spallation reactions. The production rate ratios are thus roughly uniform to depth due to very low ^{10}Be muogenic production rates, and consequently any offset to the measured $^3\text{He}/^{10}\text{Be}$ concentration

ratio is solely a function of temperature, when all other diffusion-affecting parameters are held constant. Higher- or lower-than-expected retention under any erosion type indicates that a sample experienced slightly different thermal regimes during exhumation, as compared to the thermal regime it would have experienced under uniform erosion. Our model results suggest that these differences are negligible, and that ^3He may be useful for determining long-term bedrock temperatures in cold regions undergoing stochastic erosion, provided sufficient analytical resolution.

5.2.2. Constraints on the Application of Cosmogenic ^3He as a Paleothermometer in Eroding Settings

The thermal history of any quartz-containing sample can be evaluated as long as concentrations of ^3He and ^{10}Be are high enough for measurement. In contrast to stable or very slowly eroding environments (Tremblay et al., 2014a), relatively fast erosion rates in high-mountain regions yield comparatively low nuclide concentrations. Because detection limits for ^{10}Be are low enough to allow exposure dating even on centennial timescales (e.g., Finkel et al., 2008), the limits to applicability are primarily set by ^3He concentrations. Present-day environmental temperatures at the sampling site therefore must, above all else, be cold enough to retain sufficiently high concentrations of ^3He within the quartz grains for accurate measurement (see Figure 2 and Tremblay et al., 2014a). In the European Alps, for example, this may correspond to MATs colder than 5°C , depending on the seasonal temperature amplitude and erosion rate (Figures 2 and 6). In addition to MAT, quartz grain size imparts another important control on ^3He retention (Tremblay et al., 2014a). Thus, temperatures too warm for adequate retention in small grains could, to some extent, be compensated for by selecting a larger grain size fraction for measurement.

It is also important to note that there remain considerable uncertainties in the SLHL spallogenic production rates for ^3He , as values reported in the literature vary by up to 20% (Borchers et al., 2016; Goehring et al., 2010; Vermeesch et al., 2009). Therefore, if production rates of ^3He are, in reality, higher than those employed for interpretation, the inferred paleo-temperatures would be warmer than reality, and the opposite for the case where production rates are lower than those used for interpretation. Assuming one uses the mean of measured SLHL production rates (as in Tremblay et al., 2014a, 2018), and that the range of published production rate suitably represents the bounds of the actual SLHL production rate, the maximum production rate uncertainty bounds of appx. $\pm 10\%$ corresponds to a calculated retention increase/decrease of appx. 0.08, or differences in the inferred MAT of $5\text{--}10^\circ\text{C}$, depending on the T_A , and assuming constant MAT and no erosion (Figure 2). Despite these uncertainties, however, ^3He paleothermometry can still provide useful constraints on paleoclimate conditions, and is particularly robust for comparing samples against one another (e.g., north-facing vs. south-facing hillslopes). Assuming sample-specific factors like grain size and diffusion kinetics can be corrected for, the thermal offset between two samples would persist irrespective of the SLHL production rate.

^3He retention from one single amalgamated sample does not yield a series of absolute or definitive temperatures, but instead yields one value which corresponds to the average diffusivity across the time period of integration. The retention must be evaluated in the context of a model that incorporates temperature-dependent diffusivity scaling as a function of the imposed thermal conditions (Tremblay et al., 2014a, 2018) in order to derive possible and plausible thermal histories for each sample. For samples collected from the field, one would simulate a suite of possible thermal histories to determine if it yields a retention which matches that measured for the sample. If the site is inferred to be eroding, these simulations could be informed by erosion rates estimated using ^{14}C and ^{10}Be concentrations. While we have explored relatively simple scenarios, the model presented here allows for the exploration of more complicated settings that include, for example, cracks and void spaces, or lithological variations. One could likewise impose a dampened winter thermal signal that varies from year-to-year in order to simulate seasonal snow cover, or impose temporally transient erosion rates, both of which affect production rates and the temperature conditions at depth.

5.3. Investigating Short-Term Erosional Transience and Paleoclimate Using Non-Amalgamated Samples

The primary focus of our modeling is to test how robustly erosion rates and paleo-temperatures in cold, bedrock hillslopes can be obtained over a large spatial extent and on kyr-timescales. This approach precludes a detailed evaluation of the thermal evolution or rockfall frequency-magnitude distribution of a rockwall, but rather seeks to observe the effects of temperature on erosion rates in the aggregate. Nevertheless, for a surface undergoing

spatially heterogeneous erosion, CN concentrations from individual singular samples each reflect their unique exhumation history, and can offer information about the temporal evolution of an eroding surface.

For example, the distribution of $^{14}\text{C}/^{10}\text{Be}$ ratios from samples collected across a bedrock surface reflect the predominant style of erosion. Ratios that deviate strongly, and/or non-uniformly, from the $^{14}\text{C}/^{10}\text{Be}$ ratio expected for uniform erosion, would indicate that erosion is dominated by random, stochastic events. Depending on the sensitivity of the concentration analyses, one could, in principle, even return possible rockfall event sizes, simply by having sampled the rockwall surface (see Appendix C). This is especially advantageous for high alpine regions, where falling blocks may shatter on impact, thereby reducing block sizes and impeding characterization of in-situ block sizes using the rockfall debris. Conversely, if most samples returned ratios close to the expected uniform erosion rate value, it could be inferred that erosion occurs more or less uniformly. Whereas previous studies, notably Hippe et al. (2012) and Skov et al. (2019) have explored erosional transience using ^{14}C and ^{10}Be at the catchment scale, our hypothetical rockwall example demonstrates that $^{14}\text{C}/^{10}\text{Be}$ ratios are also suitable for studying short-term, spatially constrained erosional transience.

5.4. Extending a 1D Model to 3D Problems: Sampling and Analytical Considerations

5.4.1. Considerations for Sampling a 3D Rock Surface

In our model, we parameterized the eroding surface as a perfectly flat plane which lowers through time. When tilting this surface into something more realistic, the cosmogenic nuclide attenuation lengthscales must be calculated according to the hillslope angle and the production rates must be adjusted due to the additional “self-shielding” of the rockwall surface (Dunne et al., 1999). Furthermore, along cliff faces, and particularly narrow ridges or arêtes, muogenic production may occur from both sides (depending on the hillslope angle). This renders several of the strategies outlined here impossible, as the applications for paired $^{14}\text{C}/^{10}\text{Be}$ outlined above rely strongly on the variable, but determinable, production rates for the specific production mechanisms (spallation, muon capture, etc.) in order to evaluate a sample's exhumation history. At 15 m depth in the flat surfaces modeled here, total ^{14}C production is less than 1% of the surface production rate, and total ^{10}Be is less than 0.5% (Figure 1a). These values are even lower in inclined surfaces which have lower attenuation lengths (Dunne et al., 1999). Therefore, at a minimum ridge width of 30 m, possible “double-sided production” is nearly negligible.

Likewise, complex surface geometries which deviate strongly across the sampled surface and alter the local production rates for each sub-sample may yield erroneous $^{14}\text{C}/^{10}\text{Be}$ corrections due to variable shielding and attenuation length scales, which are partially a function of slope angle (DiBiase, 2018; Dunne et al., 1999). Complicated surface geometries may additionally affect the bedrock temperature conditions due to conduction of heat from multiple directions; nevertheless, Gruber et al. (2004b) show that simplified numerical models using simplified geometries (realized in 2D in their case to reconstruct spatial permafrost distribution) can accurately simulate bedrock temperatures at depth. High-resolution ($\sim 2\text{m}$ or finer) surface digital elevation models (DEMs) which allow for a rigorous calculation of local production rates would, of course, be ideal. In the absence of this, careful sample collection in places of complex surface topography with particular attention to possible fine-scale divergences of local production rates, and alongside conservative interpretation of $^{14}\text{C}/^{10}\text{Be}$ ratios, may suffice.

Accounting for site-specific shielding is important not only for production rate calculations, but also for representing the thermal conditions below the surface. “Thermal shielding” by seasonal snow cover, for example, can significantly alter ^3He retention and is therefore a critical consideration prior to sampling, if uncertainties regarding the effect of transient features on surface temperatures are to be avoided (Tremblay et al., 2018). Finally, ensuring a spatially representative amalgamated sample is critically important. As we have shown in our model experiments, amalgamated samples which include ~ 30 sub-samples yield erosion rates which closely approximate the true erosion rate, even if the concentrations are biased up to 40% by the largest events (Figures 10–12). Furthermore, stronger biases can be corrected for (Figures 12 and 13; Section 5.1.3) if they manifest in $^{14}\text{C}/^{10}\text{Be}$ ratios.

5.4.2. Limitations on Application Due To Analytical Capabilities

As noted above, one considerable limitation to the application of ^3He as a paleothermometer is the need to determine individual He diffusion kinetics for the different quartz species used. This is a non-trivial process requiring irradiation of an aliquot of the measured quartz at high kinetic energies and subsequent diffusion experiments

with stepwise heating controls. Furthermore, in rapidly eroding settings, measurements on samples with low ^3He concentrations may yield considerable error, depending on the precision of the instruments, rendering distinctions between diverging temperature regimes difficult to parse. We note that previous applications of ^3He paleothermometry yield retention uncertainties (which incorporates uncertainties due to ^3He production and diffusion) of up to $\pm 4\%$ (Tremblay et al., 2018).

Low ^{14}C concentrations may likewise complicate $^{14}\text{C}/^{10}\text{Be}$ ratios, as the extraction protocol for ^{14}C often yields high procedural blanks. The associated uncertainty may strongly vary depending on the sample preparation and measurement protocol employed. At 2,800 m. a.s.l. (a representative elevation for permafrost rockwalls in the European Alps; Cremonese et al., 2011), the expected surface ^{14}C concentration is appx. 6.9×10^4 atoms g^{-1} . At 2 m and 4 m below the surface, the expected concentrations are appx. 7.5×10^3 atoms g^{-1} and 3.6×10^3 atoms g^{-1} respectively, assuming an erosion rate of approximately 0.1 cm yr^{-1} . Accurate measurement of these concentrations, particularly the low concentration, depends on the precision of the accelerator mass spectrometer and the sample preparation protocol. We note that samples measured with concentrations on the order of 10^5 atoms g^{-1} commonly yield measurement uncertainties on ^{14}C of less than 1%. These uncertainties are between 3% and 25% for concentrations in the 10^4 atoms g^{-1} order of magnitude, and between 8% and 64% for concentrations in the 10^3 atoms g^{-1} order of magnitude, though the range for the lowest-concentration data is based only on four samples (Lupker et al., 2015).

6. Conclusions

We have presented results from a 1D numerical model simulating the evolution of three CNs in quartz, ^{14}C , ^{10}Be , and ^3He , as well as shallow sub-surface temperatures, under a variety of erosional settings in order to evaluate their utility as proxies for ground surface temperature, erosion rate, and erosional stochasticity. Our results suggest that ^{10}Be -derived erosion rates from amalgamated samples of hillslopes undergoing stochastic erosion may underestimate the long-term erosion rate. Deviations of the measured $^{14}\text{C}/^{10}\text{Be}$ ratio from the expected $^{14}\text{C}/^{10}\text{Be}$ ratio reflect biases due to the stochastic erosion events, and can be used to correct potentially biased erosion rates, or to approximate the depth of stochastic events.

We additionally find the extension of ^3He as a useful “geothermometer” into both rapidly eroding as well as stochastically eroding landscapes. ^3He retention in quartz, when controlling for differences in erosion rate, is a function of temperature. Even in highly stochastic scenarios, ^3He retention scales near to that expected under steady-state erosion, suggesting that ^3He retention, when interpreted using a time-temperature-erosion model, can be used to derive integrated ground surface temperatures in cold, bedrock hillslopes. ^3He is therefore uniquely suitable for evaluating erosional processes in regions where temperature-dependent weathering mechanisms, like frost-weathering, are believed to exert controls on landscape evolution. These results are particularly useful for evaluating erosion rates and the temperature-dependence of erosion in landscapes where the primary mechanisms of erosion are sensitive to temperature—notably, permafrost and periglacial environments. Determining the response of these landscapes to changes in temperature is critical to anticipate both the short- and long-term effects of climate change. The cosmogenic nuclide system described here provides a quantitative constraint on erosion rate, temperature, and erosion style in these dynamic regions. Application of the methodologies discussed herein is, at present, limited primarily by analytical precision.

Appendix A: Terms and Default Model Parameter Values

Table A1 reports the terms used in the manuscript as well as the default model parameter values used in all simulations.

Table A1

Table of Terms and Default Model Parameter Values

Symbol	Name	Model components	Value	Units
P_n	Nucleogenic (spallation) production rate	$^3\text{He}/^{10}\text{Be}/^{14}\text{C}$		atoms $\text{g}^{-1} \text{yr}^{-1}$
$P_{n,^{10}\text{Be}}(0)$	^{10}Be spallation surface production rate	^{10}Be	4.01	atoms $\text{g}^{-1} \text{yr}^{-1}$
$P_{n,^{14}\text{C}}(0)$	^{14}C spallation surface production rate	^{14}C	12.8	atoms $\text{g}^{-1} \text{yr}^{-1}$
$P_{n,^3\text{He}}(0)$	^3He spallation surface production rate	^3He	114	atoms $\text{g}^{-1} \text{yr}^{-1}$
z	depth	All	0–350; 0–1,500	cm
ρ_{rock}	rock density	Temp.	2.62	g cm^{-3}
Λ_n	spallation attenuation length scale	$^3\text{He}/^{10}\text{Be}/^{14}\text{C}$	160	g cm^{-2}
P_{μ^-}	negative muon capture production rate	$^{10}\text{Be}/^{14}\text{C}$		atoms $\text{g}^{-1} \text{yr}^{-1}$
R_{μ^-}	stopping rate of negative muons	$^{10}\text{Be}/^{14}\text{C}$		$\text{g}^{-1} \text{yr}^{-1}$
B	fast muon surface production rate	^{10}Be	0.026	atoms $\text{g}^{-1} \text{yr}^{-1}$
$f_{\text{tar},^{14}\text{C}}$	probability of production from negative muon capture (^{14}C)	^{14}C	1.72×10^{-2}	
$f_{\text{tar},^{10}\text{Be}}$	probability of production from negative muon capture (^{10}Be)	^{10}Be	5.6×10^{-4}	
A_1	negative muon capture scaling factor	$^{10}\text{Be}, ^{14}\text{C}$	170.6	$\text{g}^{-1} \text{yr}^{-1}$
A_2	negative muon capture scaling factor	$^{10}\text{Be}, ^{14}\text{C}$	36.75	$\text{g}^{-1} \text{yr}^{-1}$
$\Lambda_{\mu,1}$	negative muon attenuation length scale	$^{10}\text{Be}, ^{14}\text{C}$	738.6	g cm^{-2}
$\Lambda_{\mu,2}$	negative muon attenuation length scale	$^{10}\text{Be}, ^{14}\text{C}$	2,688	g cm^{-2}
$\Lambda_{\mu,3}$	fast muon attenuation length scale	^{10}Be	4,360	g cm^{-2}
P_T	total cosmogenic nuclide production rate	$^{10}\text{Be}/^{14}\text{C}$		atoms $\text{g}^{-1} \text{yr}^{-1}$
ε	long-term erosion rate	$^3\text{He}/^{10}\text{Be}/^{14}\text{C}$		$\text{g cm}^2 \text{yr}^{-1}$
$\lambda_{^{10}\text{Be}}$	^{10}Be decay constant	^{10}Be	4.98667×10^{-7}	yr^{-1}
$\lambda_{^{14}\text{C}}$	^{14}C decay constant	^{14}C	1.2097×10^{-4}	yr^{-1}
t	time	All	0–25,000	years (a)
$C_{^{10}\text{Be}}$	^{10}Be concentration	^{10}Be		atoms g^{-1}
$^{14}\text{C}/^{10}\text{Be}$	ratio of the concentrations of ^{14}C and ^{10}Be	$^{14}\text{C}/^{10}\text{Be}$		
$C_{^3\text{He}}$	^3He concentration	^3He		atoms g^{-1}
$C_{^{14}\text{C}}$	^{14}C concentration	^{10}Be		atoms g^{-1}
$D(T)$	^3He diffusivity in quartz	^3He		$\text{cm}^2 \text{s}^{-1}$
$\ln(D_0/a^2)$		^3He	11.1	s^{-1}
E_a	^3He activation energy	^3He	84,500	J mol^{-1}
R	gas constant	^3He	8.3144	$\text{J K}^{-1} \text{mol}^{-1}$
T	temperature	^3He	253.15–293.15	K
EDT	effective diffusion temperature	^3He		K
$R_{3/10}$	^3He retention	^3He		
$T_{z_0}(t)$	Surface temperature	Temp.		K
MAT	mean annual surface temp.	Temp.		K
T_A	annual temp. amplitude	Temp.		K
α	thermal diffusivity of the bedrock	Temp.	1.5×10^{-2}	$\text{cm}^2 \text{s}^{-1}$
P_y	period of sinusoidal temperature function	Temp.	1	
h_e	depth of erosion event	$^3\text{He}/^{10}\text{Be}/^{14}\text{C}$		cm
$\varepsilon_{^{10}\text{Be}}$	measured (^{10}Be -derived) erosion rate	^{10}Be		cm yr^{-1}
ε_c	corrected erosion rate	$^{10}\text{Be}/^{14}\text{C}$		cm yr^{-1}
c	Gen. Pareto distribution shape parameter	$^3\text{He}/^{10}\text{Be}/^{14}\text{C}$	0.5, 0.7, 0.9, 0.8	
x_m	Gen. Pareto distribution scale parameter	$^3\text{He}/^{10}\text{Be}/^{14}\text{C}$	0.5, 0.3, 0.1, 0.2	

Table A1
Continued

Symbol	Name	Model components	Value	Units
M_1	Correction scaling factor 1	$^{10}\text{Be}/^{14}\text{C}$	-0.004	
M_2	Correction scaling factor 2	$^{10}\text{Be}/^{14}\text{C}$	0.031	
M_3	Correction scaling factor 3	$^{10}\text{Be}/^{14}\text{C}$	0.0988	
$\left(\frac{C_{14C}}{C_{10Be}}\right)_{OBS}$	observed $^{14}\text{C}/^{10}\text{Be}$ ratio	$^{10}\text{Be}/^{14}\text{C}$		
$\left(\frac{C_{14C}}{C_{10Be}}\right)_{UE}$	expected $^{14}\text{C}/^{10}\text{Be}$ ratio	$^{10}\text{Be}/^{14}\text{C}$		

Note. The terms “EDT”, “ ϵ_{10Be} ”, “ ϵ_c ”, “ $(C_{14C}/C_{10Be})_{obs}$ ”, and “ $(C_{14C}/C_{10Be})_{UE}$ ” are values derived by the model; all others are input parameters or variables calculated thereof.

Appendix B: Variables Tested in Model Runs

Table B1 reports the erosion rate, mean annual temperature (MAT), the seasonal temperature amplitude (T_A), the pareto shape value (c), the number of scenarios run under these conditions, and the erosion event recurrence frequency (if applicable) for all of the model runs included in the test dataset. This is the same dataset used to determine the coefficients M_1 , M_2 , and M_3 in Equation 15. Table B2 reports the values for the same variables for the correction test dataset.

Table B1
Table of Variables Tested for Each Model Run

Erosion style	Long-term erosion rate ($\pm 0.01 \text{ cm yr}^{-1}$)	MAT ($^{\circ}\text{C}$)	T_A ($^{\circ}\text{C}$)	Pareto c	Recurrence frequency (yrs)	Scenarios (No.)	Relevant Figure
No Erosion	0.0	5.0	5.0	NA	NA	1	1a
No Erosion	0.0	0.0	5.0	NA	NA	1	1a
No Erosion	0.0	-5.0	5.0	NA	NA	1	1a
No Erosion	0.0	-10.0	5.0	NA	NA	1	1a
No Erosion	0.0	-20.0	10.0	NA	NA	1	1a
No Erosion	0.0	0.0	2.5	NA	NA	1	1b
No Erosion	0.0	0.0	5.0	NA	NA	1	1b
No Erosion	0.0	0.0	10.0	NA	NA	1	1b
No Erosion	0.0	0.0	15.0	NA	NA	1	1b
No Erosion	0.0	0.0	20.0	NA	NA	1	1b
Uniform	0.01	0.0	5.0	NA	NA	1	6
Uniform	0.075	0.0	5.0	NA	NA	1	6
Uniform	0.1	0.0	5.0	NA	NA	1	6
Uniform	0.125	0.0	5.0	NA	NA	1	6
Uniform	1.0	0.0	5.0	NA	NA	1	6
Episodic	0.05	0.0	5.0	NA	100	1	7a
Episodic	0.05	0.0	5.0	NA	1,000	1	7a
Episodic	0.1	0.0	5.0	NA	100	1	7b
Episodic	0.1	0.0	5.0	NA	1,000	1	7b
Episodic	0.25	0.0	5.0	NA	100	1	7c
Episodic	0.25	0.0	5.0	NA	1,000	1	7c
Stochastic	0.05	0.0	5.0	0.7	NA	10	9a
Stochastic	0.1	0.0	5.0	0.7	NA	10	9b

Table B1

Continued

Erosion style	Long-term erosion rate (± 0.01 cm yr ⁻¹)	MAT (°C)	T_A (°C)	Pareto c	Recurrence frequency (yrs)	Scenarios (No.)	Relevant Figure
Stochastic	0.25	0.0	5.0	0.7	NA	10	9c
Stochastic	0.1	0.0	5.0	0.5	NA	10	10a
Stochastic	0.1	0.0	5.0	0.7	NA	10	10b
Stochastic	0.1	0.0	5.0	1.0	NA	10	10c

Table B2

Table of Variables for Scenarios Within the ¹⁴C/¹⁰Be Correction Test Data Set

Erosion style	Long-term erosion rate (± 0.01 cm yr ⁻¹)	MAT (°C)	T_A (°C)	Pareto c	Recurrence frequency (yrs)	Scenarios (No.)	Relevant Figure
Stochastic	0.025	0.0	5.0	0.8	NA	2	13
Stochastic	0.05	0.0	5.0	0.8	NA	2	13
Stochastic	0.075	0.0	5.0	0.8	NA	2	13
Stochastic	0.1	0.0	5.0	0.8	NA	2	13
Stochastic	0.125	0.0	5.0	0.8	NA	2	13
Stochastic	0.15	0.0	5.0	0.8	NA	2	13
Stochastic	0.175	0.0	5.0	0.8	NA	2	13
Stochastic	0.2	0.0	5.0	0.8	NA	2	13
Stochastic	0.225	0.0	5.0	0.8	NA	2	13
Stochastic	0.25	0.0	5.0	0.8	NA	2	13
Stochastic	0.275	0.0	5.0	0.8	NA	2	13
Stochastic	0.3	0.0	5.0	0.8	NA	2	13

Appendix C: Determining Apparent Erosion Event Depth Using ¹⁴C/¹⁰Be

A surface's erosion rate dictates its ¹⁴C/¹⁰Be ratio (Figure 1b), and surfaces which erode rapidly have both higher surface and subsurface ratios. The difference in ¹⁴C/¹⁰Be ratio as a function of erosion rate is due to the differential half-lives of ¹⁴C and ¹⁰Be, and particularly, the relatively short half-life of ¹⁴C (Figure C1). As noted in chapter 5.3, these factors can be exploited in order to extract information about the manner in which the surface is eroding, including the apparent depth of large erosion events.

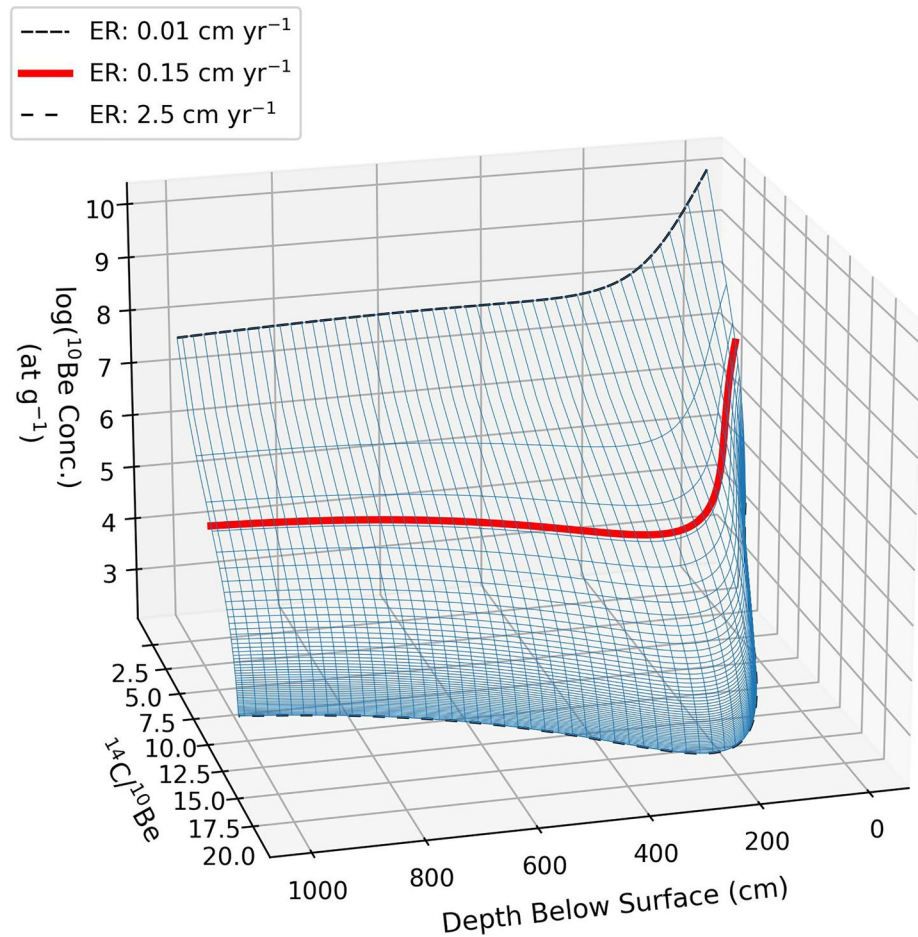


Figure C1. ^{10}Be concentration and $^{14}\text{C}/^{10}\text{Be}$ ratio at depth under steady-state erosion. The shape of the surface is set by the steady-state erosion rate. Plotted here are values for erosion rates 0.01 cm yr^{-1} to 2.5 cm yr^{-1} . The red line indicates the $^{14}\text{C}/^{10}\text{Be}$ ratio and ^{10}Be concentration at depth for an erosion rate of 0.15 cm yr^{-1} . Samples which fall on or near the plotted surface can be used to reconstruct erosion event depths, while others have concentration and/or $^{14}\text{C}/^{10}\text{Be}$ ratios which reflect a combination of erosion events, or a combination of erosion events and stasis following erosion. It is analogous to the “banana plots” of nuclides with diverging half-lives which allow surface exposure dating of samples with complex exposure histories (Gosse & Philips, 2001; Hippe et al., 2012).

Unless comparing against an independently derived erosion rate (see chapter 5.3), multiple sub-samples are necessary in order to determine the apparent depth of any individual sub-sample. Instead of combining the sub-samples into one amalgamated sample, as prescribed above for determining representative erosion rates, the ^{14}C and ^{10}Be concentrations from the individual sub-samples must be determined for each individual sub-sample. The mean nuclide concentration of all samples then corresponds to that of an amalgamated sample, while the individual concentrations reflect the sample-specific exhumation history. Table B1, Table B2.

Because cosmogenic nuclide concentrations decrease approximately exponentially in the sub-surface, and due to the different production mechanisms of ^{10}Be and ^{14}C , the combined concentration and $^{14}\text{C}/^{10}\text{Be}$ ratio reflect the depth from which material originates (Figures 1 and C1). The blue surface plotted in Figure C1 shows the expected ^{10}Be concentrations and ratios for erosion rates between 0.01 cm yr^{-1} and 1.0 cm yr^{-1} . The red line shows the expected depth, $^{14}\text{C}/^{10}\text{Be}$, ^{10}Be concentration profile for a surface eroding at approximately 0.08 cm yr^{-1} . Figure C1 is roughly analogous to the “banana plots” common in paired-nuclide exposure age calculations (e.g., Gosse & Philips, 2001; Hippe et al., 2012), though it adds a depth below the surface component.

Using data from the simulations outlined above in Chapter 4, we calculated an expected $^{14}\text{C}/^{10}\text{Be}$ ratio, a ^{10}Be concentration, and depth profile from an amalgamated sample, and then returned expected depths for samples with measured $^{14}\text{C}/^{10}\text{Be}$ ratios that deviate from the expected $^{14}\text{C}/^{10}\text{Be}$ for the ^{10}Be -derived erosion rate by more

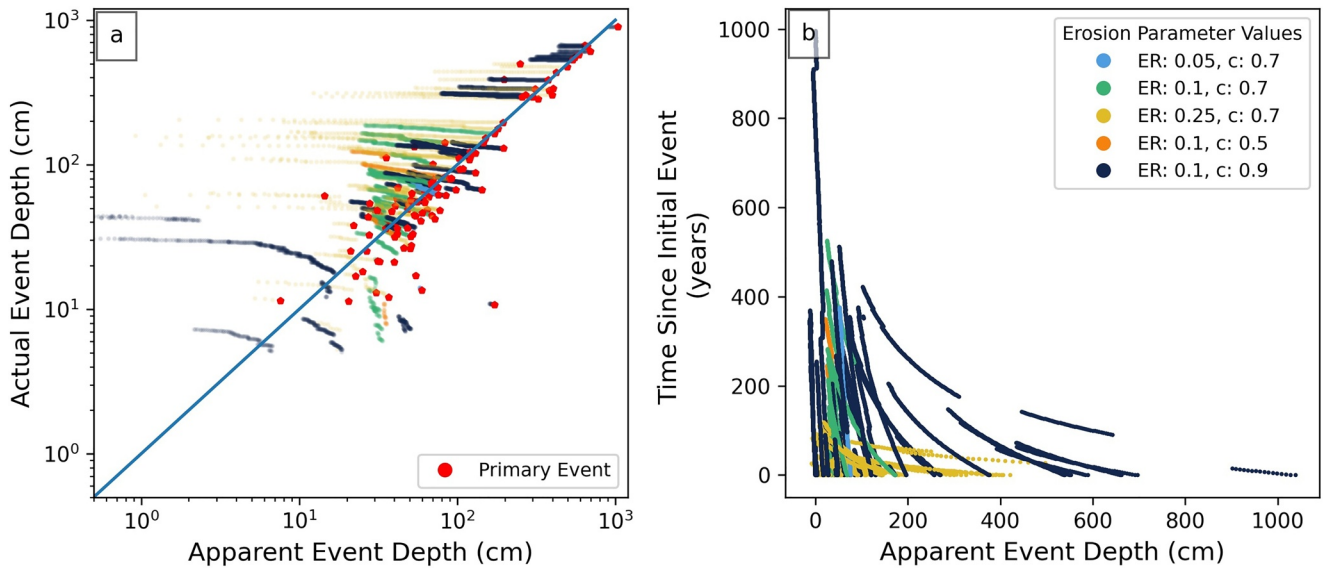


Figure C2. Erosion event depth calculated using sample $^{14}\text{C}/^{10}\text{Be}$ and ^{10}Be concentration. When individual sample $^{14}\text{C}/^{10}\text{Be}$ ratios deviate from the expected $^{14}\text{C}/^{10}\text{Be}$ of an amalgamated sample (at the ^{10}Be erosion rate), the individual sample $^{14}\text{C}/^{10}\text{Be}$ and concentration can be used to return an apparent event size (Figure C2a). The data are plotted according to erosion rate and Pareto shape value (c), reflected in the legend colors in C2b. We use a threshold deviation from the expected $^{14}\text{C}/^{10}\text{Be}$ of 2.0 to identify suitable samples. The accuracy of the prediction diminishes with time (Figure C2b) following the initial, primary event marked in red in panel a. As the concentration of cosmogenic nuclides increases and the $^{14}\text{C}/^{10}\text{Be}$ ratio attenuates to the surface production ratio, the accuracy of the apparent event size diminishes. “Trails” which do not start at time 0 after an initial event reflect large events that occurred in relatively quick succession after another large event, preventing the nuclide concentrations from “resetting” to the concentration expected under steady-state erosion.

than 1.0. Using a third-degree polynomial (multiple) linear regression fitted to the expected ^{10}Be concentration and expected $^{14}\text{C}/^{10}\text{Be}$ profiles, we can calculate the apparent event depths (Figure C2).

The accuracy of the event depth approximation is best for samples which are collected in the years immediately following very large (>appx. 50 cm) events (Figure C2a). The accuracy diminishes as the $^{14}\text{C}/^{10}\text{Be}$ ratio, which is typically higher than the surface value, attenuates to the surface production ratio. In Figure C2a, erosion events deeper than 10 cm are shown as red dots and labeled as the “primary event,” while the calculated event depths for the years that follow almost always trail behind. This is shown more clearly in Figure C2b, which demonstrates that the apparent event depth (typically) decreases as time since the event increases. In Figure C2a, the depths which appear without a “trail” of decreasing depths are those which follow another large event in rapid succession and lack enough time to attenuate to the surface ratio expected under uniform ratio.

Because of the (often considerable) inconsistency between the apparent and actual event depths, and the analytical uncertainties associated with cosmogenic nuclide measurements, the calculated apparent depths should be interpreted conservatively, typically as minimum depths, and are best suited for characterizing the erosion style in a broad sense.

Acknowledgments

This research received funding from the European Research Council under the European Union’s Horizon 2020 research and innovation programme under grant agreement 759639. We thank Benny Guralnik, Kristina Hippe, Marissa Tremblay, Maarten Lupker, Sascha Brune, and Samuel Niedermann for insightful discussions throughout the course of this work. We additionally thank Michal Ben-Israel, two additional anonymous reviewers, and editor Mikael Attal for their thoughtful and insightful comments that greatly improved the manuscript. Open access funding enabled and organized by Projekt DEAL.

Data Availability Statement

All model scripts used to generate the data and Figures 7–13 are available on as an open-access data publication via GFZ Data Services at <https://doi.org/10.5880/GFZ.3.3.2022.001>.

References

- Anderson, R. S. (1998). Near-surface thermal profiles in alpine bedrock: Implications for the frost weathering of rock. *Arctic and Alpine Research*, 30(4), 362–372. <https://doi.org/10.1080/00040851.1998.12002911>
- Bierman, P. R. (1994). Using in situ produced cosmogenic isotopes to estimate rates of landscape evolution: A review from the geomorphic perspective. *Journal of Geophysical Research*, 99, 13885–13896. <https://doi.org/10.1029/94JB00459>
- Bodin, X., Schoeneich, P., Deline, P., Ravel, L., Magnin, F., Krysiński, J.-M., & Echelard, T. (2015). Mountain permafrost and associated geomorphological processes: Recent changes in the French Alps. *Journal of Alpine Research*, 103(2). <https://doi.org/10.4000/rga.2885>

- Borchers, B., Marrero, S., Balco, G., Caffee, M., Goehring, B., Lifton, N., et al. (2016). Geological calibration of spallation production rates in the CRONUS-Earth project. *Quaternary Geochronology*, *31*, 188–198. <https://doi.org/10.1016/j.quageo.2015.01.009>
- Braucher, R., Castillo, P. D., Siame, L., Hidy, A. J., & Bourles, D. L. (2009). Determination of both exposure time and denudation rate from an in situ-produced ¹⁰Be depth profile: A mathematical proof of uniqueness. Model sensitivity and applications to natural cases. *Quaternary Geochronology*, *4*(1), 56–67. <https://doi.org/10.1016/j.quageo.2008.06.001>
- Carslaw, H. J., & Jaeger, J. C. (1959). *Conduction of heat in solids*. Oxford University Press.
- Christoudoulides, C., Ettinger, K. V., & Fremlin, J. H. (1971). The use of TL glow peaks at equilibrium in the examination of the thermal and radiation history of materials. *Modern Geology*, *2*, 275–280.
- Cremonese, E., Gruber, S., Phillips, M., Pogliotti, P., Boeckli, L., Noetzi, J., et al. (2011). Brief Communication: An inventory of permafrost evidence for the European Alps. *The Cryosphere*, *5*(3), 651–657. <https://doi.org/10.5194/tc-5-651-2011>
- Dennis, D. P., & Scherler, D. (2022). Stein - stochastic erosion in-situ cosmogenic nuclide model. *GFZ Data Services*. <https://doi.org/10.5880/GFZ.3.3.2022.001>
- DiBiase, R. (2018). Increasing vertical attenuation length of cosmogenic nuclide production on steep slopes negates topographic shielding corrections for catchment erosion rates. *Earth Surface Dynamics*, *6*(4), 923–931. <https://doi.org/10.5194/esurf-6-923-2018>
- Drury, M. J. (1987). Thermal diffusivity of some crystalline rocks. *Geothermics*, *16*(2), 105–115. [https://doi.org/10.1016/0375-6505\(87\)90059-9](https://doi.org/10.1016/0375-6505(87)90059-9)
- Dunai, T. (2010). *Cosmogenic nuclides: Principles, concepts, and applications in the Earth surface sciences*. Cambridge University Press.
- Dunne, J., Elmore, D., & Muzikar, P. (1999). Scaling factors for the rates of production of cosmogenic nuclides for geometric shielding and attenuation at depth on sloped surfaces. *Geomorphology*, *27*, 3–11. [https://doi.org/10.1016/s0169-555x\(98\)00086-5](https://doi.org/10.1016/s0169-555x(98)00086-5)
- Dussauge, C., Grasso, J.-R., & Helmstetter, A. (2003). Statistical analysis of rockfall volume distributions: Implications for rockfall dynamics. *Journal of Geophysical Research*, *108*. <https://doi.org/10.1029/2001JB000650>
- Finkel, R. C., Schafer, J. M., & Schwartz, R. (2008). Exposure dating meets history: Precise ¹⁰Be dating of very young surfaces. *Geochimica et Cosmochimica Acta*, *72*(12), A1110–A1143.
- Gallach, X., Carcaillet, J., Ravel, L., Deline, P., OgierRossi, C. M., Malet, E., et al. (2020). Climatic and structural controls on Late-glacial and Holocene rockfall occurrence in high-elevated rock walls of the Mont Blanc massif (Western Alps). *Earth Surface Processes and Landforms*, *45*(13), 3071–3091. <https://doi.org/10.1002/esp.4952>
- Gallach, X., Ravel, L., Egli, M., Brandova, D., Schaefer, M., Christl, M., et al. (2018). Timing of rockfalls in the Mont Blanc massif (Western Alps): Evidence from surface exposure dating with cosmogenic ¹⁰Be. *Landslides*, *15*(10), 1991–2000. <https://doi.org/10.1007/s10346-018-0999-8>
- Ganti, V., von HagkeScherler, C. D., Lamb, M. P., Fischer, W. W., & Avouac, J.-P. (2016). Time scale bias in erosion rates of glaciated landscapes. *Science Advances*, *2*(10). <https://doi.org/10.1126/sciadv.1600204>
- Goehring, B. M., Kurz, M. D., Balco, G., Schaefer, J. M., Licciardi, J., & Lifton, N. (2010). A reevaluation of in situ cosmogenic ³He production rates. *Quaternary Geochronology*, *5*(4), 410–418. <https://doi.org/10.1016/j.quageo.2010.03.001>
- Gosse, J. C., & Phillips, F. M. (2001). Terrestrial in situ cosmogenic nuclides: Theory and application. *Quaternary Science Reviews*, *20*(14), 1475–1560. [https://doi.org/10.1016/s0277-3791\(00\)00171-2](https://doi.org/10.1016/s0277-3791(00)00171-2)
- Granger, D. E., & Smith, A. L. (2000). Dating buried sediments using radioactive decay and muogenic production of ²⁶Al and ¹⁰Be. *Nuclear Instruments and Methods in Physics Research Section B: Beam Interactions with Materials and Atoms*, *172*(1–4), 822–826. [https://doi.org/10.1016/s0168-583x\(00\)00087-2](https://doi.org/10.1016/s0168-583x(00)00087-2)
- Gray, J. T. (1971). *Processes and rates of development of talus slopes and proglacial rock glaciers in the Ogilvie and Wernecke Mountains, central Yukon Territory*. McGill University.
- Gruber, S., Hoelzle, M., & Haerberli, W. (2004a). Permafrost thaw and destabilization of Alpine rock walls in the hot summer of 2003. *Geophysical Research Letters*, *31*(13). <https://doi.org/10.1029/2004GL020051>
- Gruber, S., Hoelzle, M., & Haerberli, W. (2004b). Rock-wall temperatures in the Alps: Modelling their topographic distribution and regional differences. *Permafrost and Periglacial Processes*, *15*(3), 299–307. <https://doi.org/10.1002/ppp.501>
- Hales, T. C., & Roering, J. J. (2005). Climate-controlled variations in scree production, Southern Alps, New Zealand. *Geology*, *33*(9), 701–704. <https://doi.org/10.1130/G21528.1>
- Hales, T. C., & Roering, J. J. (2007). Climatic controls on frost cracking and implications for the evolution of bedrock landscapes. *Journal of Geophysical Research*, *112*, F02033. <https://doi.org/10.1029/2006JF000616>
- Hales, T. C., & Roering, J. J. (2009). A frost “buzzsaw” mechanism for erosion of the eastern Southern Alps, New Zealand. *Geomorphology*, *107*(3–4), 241–253. <https://doi.org/10.1016/j.geomorph.2008.12.012>
- Hallet, B., Walder, J. S., & Stubbs, C. W. (1991). Weathering by segregation ice growth in microcracks at sustained subzero temperatures: Verification from an experimental study using acoustic emissions. *Permafrost and Periglacial Processes*, *2*(4), 283–300. <https://doi.org/10.1002/ppp.3430020404>
- Harris, C., Arenson, L. U., Christiansen, H. H., Eitzelmüller, B., Frauenfelder, R., Gruber, S., et al. (2009). Permafrost and climate in Europe: Monitoring and modelling thermal, geomorphological and geotechnical responses. *Earth-Science Reviews*, *92*(3–4), 117–171. <https://doi.org/10.1016/j.earscirev.2008.12.002>
- Heisinger, B., Lal, D., Jull, A. J. T., Kubik, P., Ivy-Ochs, S., Neumaier, S., et al. (2002). Production of selected cosmogenic radionuclides by muons: 1. Fast muons. *Earth and Planetary Science Letters*, *200*(3–4), 345–355. [https://doi.org/10.1016/s0012-821x\(02\)00640-4](https://doi.org/10.1016/s0012-821x(02)00640-4)
- Hidy, A. J., Gosse, J. C., Pederson, J. L., Mattern, J. P., & Finkel, R. C. (2010). A geologically constrained Monte Carlo approach to modeling exposure ages from profiles of cosmogenic nuclides: An example from Lees Ferry, Arizona. *Geochemistry, Geophysics, Geosystems*, *11*(9). <https://doi.org/10.1029/2010GC003084>
- Hinchliffe, S., & Ballantyne, C. K. (1999). Talus accumulation and rockwall retreat, Trotternish, Isle of Skye, Scotland. *Scottish Geographical Journal*, *115*(1), 53–70. <https://doi.org/10.1080/00369229918737057>
- Hinchliffe, S., & Ballantyne, C. K. (2009). Talus structure and evolution on sandstone mountains in NW Scotland. *The Holocene*, *19*(30), 477–486.
- Hinderer, M. (2001). Late Quaternary denudation of the Alps, valley and lake fillings and modern river loads. *Geodinamica Acta*, *14*(4), 231–263. <https://doi.org/10.1080/09853111.2001.11432446>
- Hippe, K., Jansen, J. D., Skov, D. S., Lupker, M., Ivy-Ochs, S., Kober, F., et al. (2019). Cosmogenic in situ ¹⁴C reveals rapid soil erosion with the onset of agro-pastoralism on the Andean Altiplano. *Geophysical Research Abstracts*, *21*.
- Hippe, K., Jansen, J. D., Skov, D. S., Lupker, M., Ivy-Ochs, S., Kober, F., et al. (2021). Cosmogenic in situ ¹⁴C-¹⁰Be reveals abrupt Late Holocene soil loss in the Andean Altiplano. *Nature Communications*, *12*(1), 2546. <https://doi.org/10.1038/s41467-021-22825-6>

- Hippe, K., Kober, F., Zeilinger, G., Ivy-Ochs, S., Maden, C., Wacker, L., et al. (2012). Quantifying denudation rates and sediment storage on the eastern Altiplano, Bolivia, using cosmogenic ^{10}Be , ^{26}Al , and in situ ^{14}C . *Geomorphology*, 179, 58–70. <https://doi.org/10.1016/j.geomorph.2012.07.031>
- Hoellermann, P. (1983). *Blockgletscher als Mesoformen der Periglazialstufe* (Vol. 67). Bonner Geographische Abhandlungen.
- Ivy-Ochs, S., Kerschner, H., ReutherPreusser, A. F., Heine, K., Maisch, M., Kubik, P. W., & Schlichter, C. (2008). Chronology of the last glacial cycle in the European Alps. *Journal of Quaternary Science*, 23(6–7), 559–573. <https://doi.org/10.1002/jqs.1202>
- Kant, M. A., Ammann, J., Rossi, E., Madonna, C., Höser, D., & von Rohr, P. R. (2017). Thermal properties of Central Aare granite for temperatures up to 500°C: Irreversible changes due to thermal crack formation. *Geophysical Research Letters*, 44(2), 771–776. <https://doi.org/10.1002/2016GL070990>
- Ketchum, R. A. (2005). Forward and inverse modelling of low-temperature thermochronometry data. *Reviews in Mineralogy and Geochemistry*, 58(1), 275–314. <https://doi.org/10.1515/9781501509575-013>
- Lal, D. (1987). Production of ^3He in terrestrial rocks. *Chemical Geology: Isotope Geoscience section*, 66(1–2), 89–98. [https://doi.org/10.1016/0168-9622\(87\)90031-5](https://doi.org/10.1016/0168-9622(87)90031-5)
- Lal, D. (1991). Cosmic ray labelling of erosion surfaces: In situ nuclide production rates and erosion model. *Earth and Planetary Science Letters*, 104(2–4), 424–439. [https://doi.org/10.1016/0012-821x\(91\)90220-c](https://doi.org/10.1016/0012-821x(91)90220-c)
- Larsen, I. J., Farley, K. A., Lamb, M. P., & Pritchard, C. J. (2021). Empirical evidence for cosmogenic ^3He production by muons. *Earth and Planetary Science Letters*, 562, 116825. <https://doi.org/10.1016/j.epsl.2021.116825>
- Legay, A., Magnin, F., & Ravel, L. (2021). Rock temperature prior to failure: Analysis of 209 rockfall events in the Mont Blanc massif (Western European Alps). *Permafrost and Periglacial Processes*, 32(3), 520–536. <https://doi.org/10.1002/ppp.2110>
- Lupker, M., Hippe, K., Wacker, L., Kober, F., Maden, C., Braucher, R., et al. (2015). Depth-dependence of the production rate of in situ ^{14}C in quartz from the Leymon High core, Spain. *Quaternary Geochronology*, 28, 80–87. <https://doi.org/10.1016/j.quageo.2015.04.004>
- Mair, D., Lechmann, A., Yesilyurt, S., Tikhomirov, D., Delunel, R., Vockenhuber, C., et al. (2019). Fast long-term denudation rate of steep alpine headwalls inferred from cosmogenic ^{36}Cl depth profiles. *Scientific Reports*, 9(1), 11023. <https://doi.org/10.1038/s41598-019-46969-0>
- Matsuoka, N. (2019). A multi-method monitoring of timing, magnitude, and origin of rockfall activity in the Japanese Alps. *Geomorphology*, 336, 65–76. <https://doi.org/10.1016/j.geomorph.2019.03.023>
- Matsuoka, N., & Murton, J. (2008). Frost weathering: Recent advances and future directions. *Permafrost and Periglacial Processes*, 19(2), 195–210. <https://doi.org/10.1002/ppp.620>
- Murton, J. B., Peterson, R., & Ozouf, J.-C. (2006). Bedrock fracture by ice segregation in cold regions. *Science*, 314(5802), 1127–1129. <https://doi.org/10.1126/science.1132127>
- Muzikar, P. (2019). Episodic erosion with a power law probability density, and the accumulation of cosmogenic nuclides. *Journal of Geophysical Research: Earth Surface*, 124(9), 2345–2355. <https://doi.org/10.1029/2019JF005095>
- Niedermann, S. (2002). Cosmic-ray-produced noble gases in terrestrial rocks: Dating tools for surface processes. *Reviews in Mineralogy and Geochemistry*, 47(1), 731–784. <https://doi.org/10.2138/rmg.2002.47.16>
- Noetzi, J., Hoelzle, M., & Haeblerli, W. (2003). Mountain permafrost and recent alpine rock-fall events: A GIS-based approach to determine critical factors. *Permafrost: Proceedings of the Eighth International Conference on Permafrost*, 1, 827–832.
- O'Farrell, C. R., Heimsath, A. M., Lawson, D., Jorgensen, L. M., Evenson, E. B., Larson, G., & Denner, J. (2009). Quantifying periglacial erosion: Insights on a glacial sediment budget, matanuska glacier, Alaska. *Earth Surface Processes and Landforms*, 34(15), 2008–2022. <https://doi.org/10.1002/esp.1885>
- Olyphant, G. (1983). Analysis of the factors controlling cliff burial by talus within Blanca Massif, southern Colorado, U.S.A. *Arctic and Alpine Research*, 1(15), 65–75. <https://doi.org/10.2307/1550982>
- Pedregosa, F., Varoquaux, G., Gramfort, A., Michel, V., Thirion, B., Grisel, O., et al. (2011). Scikit-learn: Machine Learning in Python. *Journal of Machine Learning Research*, 12(85), 2825–2830.
- PERMOS: Permafrost in Switzerland. (2000/2001). Glaciological report (Permafrost), No 2/3, eds.: Vonder Mühll, D., Noetzi, J., Makowski, K., & Delaloye, R.
- Ravel, L., & Deline, P. (2011). Climate influence on rockfalls in high-Alpine steep rockwalls: The north side of the Aiguilles de Chamonix (Mont Blanc massif) since the end of the 'Little Ice Age. *The Holocene*, 21(2), 357–365. <https://doi.org/10.1177/0959683610374887>
- Reiss, R.-D., & Thomas, M. (1997). *Statistical analysis of extreme values*. Birkhäuser.
- Sanders, J. W., Cuffey, K. M., MacGregor, K. R., & Collins, B. D. (2013). The sediment budget of an alpine cirque. *GSA Bulletin*, 125(1–2), 229–248. <https://doi.org/10.1130/B30688.1>
- Sarr, A.-C., Mugnier, J.-L., Abrahami, R., Carcaillet, J., & Ravel, L. (2019). Sidewall erosion: Insights from in situ-produced ^{10}Be concentrations measured on supraglacial clasts (Mont Blanc massif, France). *Earth Surface Processes and Landforms*, 44(10), 1930–1944. <https://doi.org/10.1002/esp.4620>
- Sass, O., & Wollny, K. (2001). Investigations regarding alpine talus slopes using ground-penetrating radar (GPR) in the Bavarian Alps, Germany. *Earth Surface Processes and Landforms*, 26(10), 1071–1086. <https://doi.org/10.1002/esp.254>
- Savi, S., Comiti, F., & Strecker, M. (2021). Pronounced increase in slope instability linked to global warming: A case study from the Eastern Alps. *Earth Surface Processes and Landforms*, 46(7), 1328–1347. <https://doi.org/10.1002/esp.5100>
- Scherler, D. (2014). Climatic limits to headwall retreat in the Khumbu Himalaya, eastern Nepal. *Geology*, 42(11), 1019–1022. <https://doi.org/10.1130/g35975.1>
- Shuster, D. L., & Farley, K. A. (2005). Diffusion kinetics of proton-induced ^{21}Ne , ^3He , ^4He in quartz. *Geochimica et Cosmochimica Acta*, 69(9), 2349–2359. <https://doi.org/10.1016/j.gca.2004.11.002>
- Siewert, M. B., Krautblatter, M., Christiansen, H. H., & Eckerstorger, M. (2012). Arctic rockwall retreat rates estimated using laboratory-calibrated ERT measurements of talus cones in Longyearfjorden, Svalbard. *Earth Surface Processes and Landforms*, 37(14), 1542–1555. <https://doi.org/10.1002/esp.3297>
- Skov, D. S., Egholm, D. L., Jansen, J. D., Sandiford, M., & Knudsen, M. F. (2019). Detecting landscape transience with in situ cosmogenic ^{14}C and ^{10}Be . *Quaternary Geochronology*, 54, 101008. <https://doi.org/10.1016/j.quageo.2019.101008>
- Small, E. E., Anderson, R. S., Repka, J. L., & Finkel, R. (1997). Erosion rates of alpine bedrock summit surfaces deduced from in situ Be-10 and Al-26. *Earth and Planetary Science Letters*, 150(3–4), 413–425. [https://doi.org/10.1016/S0012-821X\(97\)00092-7](https://doi.org/10.1016/S0012-821X(97)00092-7)
- Stark, C. P., & Hovius, N. (2001). The characterization of landslide size distributions. *Geophysical Research Letters*, 28(6), 1091–1094. <https://doi.org/10.1029/2000gl008527>
- Stone, J. O. H., Evans, J. M., Fifield, L. K., Allan, G. L., & Cresswell, R. G. (1998). Cosmogenic chlorine-36 production in calcite by muons. *Geochimica et Cosmochimica Acta*, 62(3), 433–445. [https://doi.org/10.1016/s0016-7037\(97\)00369-4](https://doi.org/10.1016/s0016-7037(97)00369-4)

- Tremblay, M., Shuster, D. L., & Balco, G. (2014a). Cosmogenic noble gas paleothermometry. *Earth and Planetary Science Letters*, *400*, 195–205. <https://doi.org/10.1016/j.epsl.2014.05.040>
- Tremblay, M., Shuster, D. L., & Balco, G. (2014b). Diffusion kinetics of ^3He and ^{21}Ne in quartz and implications for cosmogenic noble gas paleothermometry. *Geochimica et Cosmochimica Acta*, *142*, 186–204. <https://doi.org/10.1016/j.gca.2014.08.010>
- Tremblay, M., Shuster, D. L., Spagnolo, M., Renssen, H., and Ribolini, A. (2018). Temperatures recorded by cosmogenic noble gases since the last glacial maximum in the Maritime Alps. *Quaternary Research*, *91*(2), 829–847. <https://doi.org/10.1017/qua.2018.109>
- Vermeesch, P., Baur, H., Heber, V. S., Kober, F., Oberholzer, P., Schaefer, J. M., et al. (2009). Cosmogenic ^3He and ^{21}Ne measured in quartz targets after one year of exposure in the Swiss Alps. *Earth and Planetary Science Letters*, *284*(3–4), 417–425. <https://doi.org/10.1016/j.epsl.2009.05.007>
- Virtanen, P., Gommers, R., Oliphant, T. E., Haberland, M., Reddy, T., Cournapeau, D., et al. (2020). SciPy 1.0: Fundamental Algorithms for Scientific Computing in Python. *Nature Methods*, *17*(3), 261–272. <https://doi.org/10.1038/s41592-019-0686-2>
- von Blanckenburg, F., & Willenbring, J. (2014). Cosmogenic nuclides: Dates and rates of Earth-surface change. *Elements*, *10*(5), 34–346. <https://doi.org/10.2113/gselements.10.5.341>
- Walder, J., & Hallet, B. (1985). A theoretical model of the fracture of rock during freezing. *The Geological Society of America Bulletin*, *96*(3), 336–346. [https://doi.org/10.1130/0016-7606\(1985\)96<336:atmotf>2.0.co;2](https://doi.org/10.1130/0016-7606(1985)96<336:atmotf>2.0.co;2)
- Ward, D. J., & Anderson, R. S. (2011). The use of ablation-dominated medial moraines as samplers for ^{10}Be -derived erosion rates of glacier valley walls, Kichatna Mountains, AK. *Earth Surface Processes and Landforms*, *36*(4), 495–512. <https://doi.org/10.1002/esp.2068>
- Wittmann, H., von Blanckenburg, F., Kruesmann, T., Norton, K. P., & Kubik, P. W. (2007). Relation between rock uplift and denudation from cosmogenic nuclides in river sediment in the Central Alps of Switzerland. *Journal of Geophysical Research*, *112*, F04010. <https://doi.org/10.1029/2006JF000729>
- Wood, J. L., Harrison, S., & Reinhardt, L. (2015). Landslide inventories or climate impacts research in the European Alps. *Geomorphology*, *228*, 398–408. <https://doi.org/10.1016/j.geomorph.2014.09.005>
- Yanites, B. J., Tucker, G. E., & Anderson, R. S. (2009). Numerical and analytical models of cosmogenic radionuclide dynamics in landslide-dominated drainage basins. *Journal of Geophysical Research*, *114*, F01007. <https://doi.org/10.1029/2008JF001088>